Iranian Journal of Numerical Analysis and Optimization
Vol. 16, No. 2, 2026, pp 607–637
https://doi.org/10.22067/ijnao.2026.96617.1784
https://ijnao.um.ac.ir/

Research Article

Fitted-mesh cubic spline methods for layer-dominated singularly perturbed parabolic problems with nonsmooth data

S.L. Cheru*, G.F. Duressa and T.B. Mekonnen

Abstract

This paper introduces a numerical framework for addressing a two-parameter singularly perturbed parabolic problems characterized by discontinuities in both the convection coefficients and the source terms. The presence of these discontinuities alongside small perturbation parameters creates distinct boundary and interior layers, which present considerable obstacles to obtaining precise numerical approximations. To address these difficulties, a layer-adapted(Shishkin-type) spatial mesh is constructed a priori, providing enhanced resolution in regions where steep solution gradients occur. The suggested method uses the implicit Euler scheme for time integration and a cubic spline in tension for spatial discretization on a

*Corresponding author

Received 21 November 2025; revised 27 January 2026; accepted 29 January 2026

Shegaye Lema Cheru
Department of Mathematics, College of Natural and Computational Sciences, Wollega University, Ethiopia.
e-mail: shegayel@wollegauniversity.edu.et

Gemechis File Duressa
Department of Mathematics, College of Natural and Computational Sciences, Jimma University, Ethiopia.
e-mail: gammeef@gmail.com

Tariku Birabasa Mekonnen
Department of Mathematics, College of Natural and Computational Sciences, Wollega University, Ethiopia.
e-mail: seenaa29@gmail.com

How to cite this article
Cheru, S.L., Duressa, G.F. and Mekonnen, T.B., Fitted-mesh cubic spline methods for layer-dominated singularly perturbed parabolic problems with nonsmooth data. *Iran. J. Numer. Anal. Optim.*, 2026; 16(2): 607-637. https://doi.org/10.22067/ijnao.2026.96617.1784

Shishkin-type mesh. A thorough analysis shows that the method achieves first-order in time and second-order up to a logarithmic factor in space when using the maximum norm, regardless of how big the perturbation parameters are. The method is especially good for modeling real-world processes like heat and mass transfer in layered media, pollutant dispersion in mixed environments, and viscous flow through composite channels, where there are often discontinuities and strong layer behavior.

AMS subject classifications (2020): 35G05, 35K20, 35K51, 65M06, 65M50.

Keywords: Singular perturbations; Two parameters; Discontinuous data; Uniform convergence; Boundary layer; Interior layer

1 Introduction

In fluid dynamics, getting the boundary and interior layer phenomena (see [14, 24]) is still a big problem for numerical modeling of complicated transport processes. These layers, usually caused by strong convection, diffusion imbalance, or reactive effects, have a big effect on how accurate and stable computational results are in real-world situations. In this research, we conduct a comprehensive numerical analysis of two-parameter singularly perturbed parabolic problems (TP-SPPPs) that represent these complex behaviors. The main goal is to build a strong and parameter uniform numerical framework that can accurately resolve sharp gradients and stay stable across the whole space-time domain. We now recall the following TP-SPPP:

$$
\begin{cases}
\mathcal{L}_{\varepsilon,\theta} w(x,t) :\equiv \left(\varepsilon \dfrac{\partial^2 w}{\partial x^2} + \theta a \dfrac{\partial w}{\partial x} - bw - c\dfrac{\partial w}{\partial t} = f \right)(x,t), (x,t) \in \mathfrak{D}^- \cup \mathfrak{D}^+, \\
\qquad w(0,t) = \mathcal{B}(t) \quad \text{in} \quad \mathfrak{D}_l, \quad w(1,t) = \mathcal{R}(t) \quad \text{in} \quad \mathfrak{D}_r, \\
\qquad w(x,0) = \mathcal{I}(x) \quad \text{in} \quad \mathfrak{D}_b, \\
\qquad |[a]\,(s)| \le C, \quad |[f]\,(s)| \le C, \\
\qquad a(x,t) \le -\theta_1 < 0, (x,t) \in \mathfrak{D}^-, a(x,t) \ge \theta_2 > 0, (x,t) \in \mathfrak{D}^+, \\
\qquad b(x,t) \ge \gamma > 0, \quad c(x,t) \ge c > 0,
\end{cases}
\tag{1}
$$

where $0 < \varepsilon \ll 1$ and $0 \le \theta \le 1$ are perturbation parameters, with domains $\mathfrak{D} = \Omega \times \Lambda$, $\mathfrak{D}^{\pm} = \Omega^{\pm} \times \Lambda$, and $\mathbb{M} = \overline{\mathfrak{D}} \setminus \mathfrak{D}$; here $\Omega = (0,1)$, $\Omega^- = (0,s)$, $\Omega^+ = (s,1)$. The boundaries are $\mathfrak{D}_l = \{(0,t) : 0 \le t \le T\}$, $\mathfrak{D}_r = \{(1,t) : 0 \le t \le T\}$, and $\mathfrak{D}_b = \mathfrak{D}_b^- \cup \mathfrak{D}_b^+$, where $\mathfrak{D}_b^- = [0,s] \times \{t = 0\}$, $\mathfrak{D}_b^+ = [s,1] \times \{t = 0\}$. Moreover, $\mathbb{M} = \mathfrak{D}_b \cup \mathfrak{D}_l \cup \mathfrak{D}_r$ and $\mathbb{M}^{\pm} = \{(s,t) : 0 \le t \le T\}$.

The coefficients $a(x,t)$ and $f(x,t)$ are assumed to be smooth in $(\mathfrak{D}^- \cup \mathfrak{D}^+) \cup \mathfrak{D}$, whereas $b(x,t)$ and $c(x,t)$ remain continuous in $\mathfrak{D}$. The inequalities $|[a]\,(s)| \leq C$ and $|[f]\,(s)| \leq C$ in (1) are used to bound the magnitude of the jump discontinuities of $a(x,t)$ and $f(x,t)$ at interior discontinuity point s. At the interface $x = s \in \Omega$, both $a(x,t)$ and $f(x,t)$ possess a jump discontinuity, denoted by $[\psi](s,t) = \psi(s^+,t) - \psi(s^-,t)$, where $\psi(s^\pm,t) = \lim_{x \to s \pm 0} \psi(x,t)$. A valid solution persists even if $a(x,t)$ changes sign across the interface, indicating opposite convection directions on each side. The solution to (1) exhibits boundary layers caused by ε, θ and an interior layer around $x = s$ resulting from discontinuities in $a(x,t)$ and $f(x,t)$. The structure and thickness of these layers depend on the ratio between the diffusion parameter and the square of the convection coefficient, as well as the sign pattern of $a(x,t)$. As a result, the thickness of the boundary layers changes, and symmetric interior layers form near $x = s$. This kind of behavior often happens in systems with convection-dominated transport and reactive flow, which shows how important it is to use parameter-uniform numerical schemes [25, 22].

The problem admits two notable limiting cases: The reaction-diffusion case ($\theta = 0$) and the convection-diffusion case ($\theta = 1$), both of which can emerge as particular forms of a general TP-SPPP model. When $\theta = 0$, boundary layers develop symmetrically on both ends of the domain, each with an approximate thickness of $O(\sqrt{\varepsilon})$. In contrast, when $\theta = 1$, the boundary layer forms near either the left or right boundary, depending primarily on the sign of the convection coefficient, and has a characteristic width of $O(\varepsilon)$. If the problem involves a discontinuous source term while $a(x,t) > 0$ (or $a(x,t) < 0$), then the solution exhibits weak interior layers for any small ε. However, when the convection coefficient itself is discontinuous such as $a(x,t) < 0$ for $x < s$ and $a(x,t) > 0$ for $x > s$, strong interior layers appear within the domain. A detailed analysis of this particular case ($\theta = 1$) can be found in [19], where the sign change of the convection coefficient is shown to shift the location of the layers within the solution.

Several researchers have contributed to the numerical analysis of TP-SPPPs, both with and without delay, employing a variety of numerical approaches (see, for instance, [9, 7, 10, 13, 16, 18, 5]). Despite these advancements, the numerical treatment of TP-SPPPs involving discontinuous convection coefficients and source terms remains at a relatively early stage of development. Chandru, Das, and Ramos [1] proposed a nearly first-order uniformly convergent scheme for (1), effectively addressing small diffusion and convection parameters with discontinuities in both convection and source terms, by combining an implicit Euler time discretization with an upwind spatial scheme. Further improvement was made by Chandru et al. [2], who designed a nearly first-order parameter-uniform scheme incorporating an adaptive mesh to enhance spatial resolution near layer regions. Kumar and Kumari [15] developed a related approach using the Crank–Nicolson method for temporal discretization on a uniform mesh and an upwind scheme on a Shishkin mesh for spatial discretization. More recently, Singh, Choudhary, and Kumar

[26] introduced a spline-based numerical method for TP-SPPPs with discontinuous convection and source terms, employing the Crank–Nicolson scheme in time coupled with trigonometric spline approximations in space. The results of these investigations overall illustrate continuous advancement in the development of resilient, parameter-consistent algorithms proficient in effectively addressing boundary and interior layers in scenarios involving discontinuous data.

In real-world scenarios like heat and mass transfer in composite materials, groundwater flow through stratified media, and pollutant transport with sudden source variations, TP-SPPPs with discontinuous convection and source terms frequently occur. Strong boundary and interior layers are induced by these discontinuities, making precise computation and analysis difficult. In order to solve this, a hybrid numerical framework is created that combines a cubic spline approximation in space over a Shishkin mesh with the implicit Euler method in time. Even in the face of extreme discontinuities, stability, accuracy, and parameter-uniform convergence are guaranteed by the adaptive mesh's ability to capture steep gradients [23, 2, 19, 6].

Fitted mesh techniques for TP-SPPPs with nonsmooth or discontinuous data are still rarely studied, despite their practical importance. The majority of current research ignores strongly perturbed cases in favor of smooth or piecewise continuous coefficients. The suggested scheme uses a Shishkin-type uniform mesh in conjunction with a cubic spline in tension, which provides high accuracy and robustness, in contrast to traditional layer-adapted approaches that depend on intricate mesh adjustments. This approach fills a significant gap in the existing numerical literature by effectively resolving sharp boundary and interior layers while preserving computational simplicity.

2 Properties of the continuous solution

This section elaborates on the derivative bounds of (1), which are essential for the ensuing numerical analysis. It is assumed in this work that the solution of (1) is uniformly bounded with respect to the perturbation parameter. Farrell *et al.* [11] previously studied the parabolic case corresponding to $\theta = 1$, while O'Riordan and Shishkin [21] studied the steady-state formulation with $\theta = 0$. We now introduce the following lemma, which, under the given assumptions, ensures the existence of a solution to (1):

Lemma 1 (Existence of solution)**.** The solution $w(x,t)$ of (1) satisfies $w \in C^0\left(\overline{\mathfrak{D}}\right) \cap C^1(\mathfrak{D}) \cap C^2(\mathfrak{D}^- \cup \mathfrak{D}^+)$.

Proof. Let w_1 and w_2 denote the solutions of SPPs [15, 26, 3, 1]:

$$\varepsilon w_{1xx} + \theta a_1 w_{1x} - b w_1 - c w_{1t} = f, \quad (x,t) \in \mathfrak{D}^-,$$
$$\varepsilon w_{2xx} + \theta a_2 w_{2x} - b w_2 - c w_{2t} = f, \quad (x,t) \in \mathfrak{D}^+,$$

where $a_1, a_2 \in C^2(\mathfrak{D})$ satisfy $a_1(x,t) < 0$ in $\mathfrak{D}^-$ and $a_2(x,t) > 0$ in $\mathfrak{D}^+$. The composite function

$$w(x,t) = \begin{cases} w_1(x,t) + \Lambda_1 \Xi_2(x,t), & (x,t) \in \mathfrak{D}^-, \\ w_2(x,t) + \Lambda_2 \Xi_1(x,t), & (x,t) \in \mathfrak{D}^+, \end{cases}$$

satisfies (1), where Ξ_1, Ξ_2 are solutions of homogeneous auxiliary problems associated with (1). The constants Λ_1 and Λ_2 are obtained by enforcing continuity of w and w_x at $x = s$:

$$w(s^-,t) = w(s^+,t), \qquad w_x(s^-,t) = w_x(s^+,t).$$

These yield a linear system whose coefficient matrix has a nonzero determinant, due to the monotonic nature of Ξ_1 and Ξ_2. Hence, unique constants Λ_1, Λ_2 exist, ensuring that $w(x,t)$ and $w_x(x,t)$ remain continuous across the interface $x = s$. □

Lemma 2 (Continuity at the interface)**.** At the discontinuity point $x = s$, the solution $w(x,t)$ and its spatial derivative are continuous, that is,

$$w(s^-,t) = w(s^+,t), \qquad w'(s^-,t) = w'(s^+,t).$$

Proof. A detailed proof is provided in [6].

□

The operator $\mathcal{L}_{\varepsilon,\theta}$ of (1) satisfies maximum principle on $\overline{\mathfrak{D}}$ as follows.

Lemma 3 (Comparison Principle)**.** Let $w \in C^0(\overline{\mathfrak{D}}) \cap C^1(\mathfrak{D}) \cap C^2(\mathfrak{D}^- \cup \mathfrak{D}^+)$ satisfy

$$w(0,t) \geq 0, \quad w(1,t) \geq 0, \quad w(x,0) \geq 0, \quad [w'](s,t) \geq 0,$$

and $\mathcal{L}_{\varepsilon,\theta} w(x,t) \geq 0$ for all $(x,t) \in \mathfrak{D}$. Then $w(x,t) \leq 0$ for every $(x,t) \in \overline{\mathfrak{D}}$.

Proof. Define an auxiliary function

$$w(x,t) = e^{-\theta\theta|x-s|/(2\varepsilon)}\, \mathcal{V}(x,t), \qquad \theta = \min\{\theta_1, \theta_2\}.$$

Substituting this into (1) yields, for $x \in \mathfrak{D}^-$,

$$\mathcal{L}_{\varepsilon,\theta} w = e^{-\theta_1\theta(s-x)/(2\varepsilon)} \Big(\varepsilon \mathcal{V}_{xx} + \theta(\theta_1 + a_1)\mathcal{V}_x + \Big[\tfrac{\theta_1\theta^2}{2\varepsilon} \Big(\tfrac{\theta_1}{2} + a_1 \Big) - b \Big] \mathcal{V} - c\mathcal{V}_t \Big),$$

and for $x \in \mathfrak{D}^+$,

$$\mathcal{L}_{\varepsilon,\theta} w = e^{-\theta_2\theta(x-s)/(2\varepsilon)} \Big(\varepsilon \mathcal{V}_{xx} + \theta(a_2-\theta_2)\mathcal{V}_x + \Big[\tfrac{\theta_2\theta^2}{2\varepsilon} \Big(\tfrac{\theta_2}{2} - a_2 \Big) - b \Big] \mathcal{V} - c\mathcal{V}_t \Big).$$

Let $(\chi,\tau) \in \overline{\mathfrak{D}}$ be the point where $\mathcal{V}$ attains its maximum. If $\mathcal{V}(\chi,\tau) \le 0$, then the claim is immediate. Otherwise, assume $\mathcal{V}(\chi,\tau) > 0$. Applying the maximum principle, (χ,τ) must lie in $\mathfrak{D}^-$, $\mathfrak{D}^+$, or at $x = s$. For interior points, $\mathcal{V}_x = \mathcal{V}_t = 0$, $\mathcal{V}_{xx} < 0$, and since $a_1 \le \theta_1 < 0$ and $a_2 \ge \theta_2 > 0$, it follows that $\mathcal{L}_{\varepsilon,\theta} w(\chi,\tau) < 0$, contradicting the assumption $\mathcal{L}_{\varepsilon,\theta} w \ge 0$. At $x = s$, the continuity of w and the conditions $[\mathcal{V}] = 0$ and $[\mathcal{V}_x] \le 0$ imply $[w_x](s,\tau) \le 0$, again a contradiction. Hence, $w(x,t) \le 0$ in $\overline{\mathfrak{D}}$. □

Lemma (3) immediately establishes the corresponding stability result, thereby ensuring the uniqueness of the solution.

Lemma 4. Let $w(x,t)$ be the solution of (1). Then

$$\|w\|_{\overline{\mathfrak{D}}} \le \mathbb{C} \max\left\{ \|\mathcal{B}\|_{\mathfrak{D}_l}, \|\mathcal{R}\|_{\mathfrak{D}_r}, \|\mathcal{I}\|_{\mathfrak{D}_b} \right\} + \frac{1}{\mathcal{S}} \|\mathcal{L}_{\varepsilon,\theta} w\|_{(\mathfrak{D}^- \cup \mathfrak{D}^+)}, \tag{2}$$

where $\mathcal{S} = \min\left\{ \frac{\theta_1}{s}, \frac{\theta_2}{1-s} \right\}$.

Proof. The proof is derived by applying Lemma (3) in conjunction with appropriately constructed barrier functions (refer to [15, 26, 4, 6]).

□

Lemma 5. Let $\theta = \min\{\theta_1, \theta_2\}$ and $\mathfrak{B} = \min_{\mathfrak{D}^- \cup \mathfrak{D}^+} \left\{ \frac{b(x,t)}{a(x,t)} \right\}$. For $1 \le \kappa + 2\iota \le 3$. Then $w(x,t)$ of (1) and its derivatives satisfy the following conditions:

1. If $\theta\theta^2 \le \mathfrak{B}\varepsilon$, then

$$\begin{aligned} \left\| \frac{\partial^{\kappa+\iota} w}{\partial x^\kappa \partial t^\iota} \right\|_{\mathfrak{D}^- \cup \mathfrak{D}^+} \le & \frac{C}{(\sqrt{\varepsilon})^\kappa} \max\Bigg\{ \|w\|_{\overline{\mathfrak{D}}}, \sum_{i+2j=0}^{2} \left(\sqrt{\varepsilon}\right)^i \left\| \frac{\partial^{i+j} \varpi}{\partial x^i \partial t^j} \right\|, \\ & \sum_{i=0}^{4} \left[\left(\sqrt{\varepsilon}\right)^i \left\| \frac{d^i \mathcal{I}}{dx^i} \right\|_{\mathfrak{D}_b} + \left\| \frac{d^i \mathcal{B}}{dt^i} \right\|_{\mathfrak{D}_l} + \left\| \frac{d^i \mathcal{R}}{dt^i} \right\|_{\mathfrak{D}_r} \right] \Bigg\}, \end{aligned}$$

2. If $\theta\theta^2 \ge \mathfrak{B}\varepsilon$, then

$$\left\| \frac{\partial^{\kappa+\iota} w}{\partial x^\kappa \partial t^\iota} \right\|_{\mathfrak{D}^- \cup \mathfrak{D}^+} \leq C \left(\frac{\theta}{\varepsilon}\right)^\kappa \left(\frac{\theta^2}{\varepsilon}\right)^\iota \max \Bigg\{ \|w\|_{\overline{\mathfrak{D}}}, \sum_{i+2j=0}^{2} \frac{\varepsilon^{i+j+1}}{\theta^{i+2j+2}} \left\| \frac{\partial^{i+j} \varpi}{\partial x^i \partial t^j} \right\|, \sum_{i=0}^{4} \left[\left(\frac{\varepsilon}{\theta}\right)^i \left\| \frac{d^i \mathcal{I}}{dx^i} \right\|_{\mathfrak{D}_b} + \left\| \frac{d^i \mathcal{B}}{dt^i} \right\|_{\mathfrak{D}_l} + \left\| \frac{d^i \mathcal{R}}{dt^i} \right\|_{\mathfrak{D}_r} \right] \Bigg\},$$

where C depends only on the coefficients and their derivatives.

Proof. For a detailed proof, the reader is referred to [15, 3]. □

Lemma 6. The solution $w(x,t)$ of (1) satisfies the bounds for second order time derivative

$$\|w_{tt}\|_{\mathfrak{D}} \leq \begin{cases} C & \text{if} \quad \theta\theta^2 \leq \mathfrak{B}\varepsilon, \\ C\theta^{-4}\varepsilon^{-2} & \text{if} \quad \theta\theta^2 \geq \mathfrak{B}\varepsilon. \end{cases}$$

Proof. This result stems from Lemma (5) and the methods presented by Gracia, O'Riordan, and Pickett [12] and O'Riordan, Pickett, and Shishkin [20]. □

3 Numerical illustrations

This section begins by semi-discretizing the problem in time on a uniform mesh, followed by approximating the spatial variable using *cubic splines in compression* over a piecewise uniform mesh, providing a stable and accurate numerical scheme.

3.1 Time variable discretization

To discretize in time, a uniform mesh is introduced over the interval $[0,T]$ with step size Δt, dividing the interval into $M = T/\Delta t$ equal subintervals. The mesh is denoted by $\Omega^M = \left\{ t_j = j\Delta t : j = 0, 1, \ldots, M,\ \Delta t = \frac{T}{M} \right\}$. Time integration is performed using the *implicit Euler method*, yielding the semi-discrete form of problem (1) on Ω^M:

$$
\begin{aligned}
&- c^{j+1}(x) D_t^- W^{j+1}(x) + \varepsilon \left(W^{j+1}\right)_{xx}(x) + \theta a^{j+1}(x) \left(W^{j+1}\right)_x(x) \\
&- b^{j+1}(x) W^{j+1}(x) = f^{j+1}(x), \qquad x \in \Omega^s, \quad 0 \le j \le M-1, \\
&W^{j+1}(0) = \mathcal{B}(t_{j+1}), \quad W^{j+1}(1) = \mathcal{R}(t_{j+1}), \\
&W^0(x) = \mathcal{I}(x), \quad x \in \overline{\mathfrak{D}},
\end{aligned}
$$

where $W^{j+1}(x)$ approximates $w(x, t_{j+1})$, and $D_t^- W^{j+1}(x) = \frac{W^{j+1}(x) - W^j(x)}{\Delta t}$ is the backward difference operator. Rewrite the above equation as

$$
\begin{cases}
\mathcal{L}^M_{\varepsilon,\theta} W^{j+1}(x) = \mathcal{G}^{j+1}(x), & x \in \Omega^s,\ 0 \le j \le M-1, \\
W^{j+1}(0) = \mathcal{B}(t_{j+1}), \quad W^{j+1}(1) = \mathcal{R}(t_{j+1}), & 0 \le j \le M-1, \\
\qquad W^0(x) = \mathcal{I}(x), & x \in \overline{\mathfrak{D}},
\end{cases}
\tag{3}
$$

where the operator $\mathcal{L}^M_{\varepsilon,\theta}$ is defined as

$$
\mathcal{L}^M_{\varepsilon,\theta} \equiv \varepsilon \frac{d^2}{dx^2} + \theta a^{j+1}(x) \frac{d}{dx} - \left(b^{j+1}(x) + \frac{c^{j+1}(x)}{\Delta t} \right) I, \quad \text{and}
$$

$$
\mathcal{G}^{j+1}(x) = f^{j+1}(x) - \frac{c^{j+1}(x)}{\Delta t} W^j(x).
$$

The local truncation error (LTE) in the temporal semi-discretization of (3) is defined as $\mathcal{E}_{j+1} = W^{j+1}(x) - \overline{\mathcal{U}}(x)$, where $\overline{\mathcal{U}}(x)$ solves

$$
\begin{cases}
\mathcal{L}_{\varepsilon,\theta} \overline{\mathcal{U}}(x) = \varpi(x, t_{j+1}) - \frac{c(x,t_{j+1})}{\Delta t} W^j(x), & x \in \Omega^s,\ 0 \le j \le M-1, \\
\overline{\mathcal{U}}(0) = \mathcal{B}(t_{j+1}), \quad \overline{\mathcal{U}}(1) = \mathcal{R}(t_{j+1}), & 0 \le j \le M-1, \\
\overline{\mathcal{U}}(x) = \mathcal{I}(x), & x \in \overline{\mathfrak{D}}.
\end{cases}
$$

The following lemma provides bounds for the LTE and the cumulative global error, following the approach in [15].

Lemma 7. Let $\mathcal{E}_{j+1}$ denote the LTE and let $\mathbb{E}_j = \sum_{\iota=1}^{j} \mathcal{E}_\iota$ be the global error up to time t_j. Then,

$$
\|\mathcal{E}_{j+1}\| \le C \Delta t^2, \quad \|\mathbb{E}_j\| \le C \Delta t, \quad 0 \le j \le M,
\tag{4}
$$

where C is a positive constant independent of ε and θ.

Proof. The first inequality in (4) follows from [26, 3]. For the global error

$$\|\mathbb{E}_j\| = \Big\| \sum_{\iota=1}^{j} \mathcal{E}_\iota \Big\| \le \sum_{\iota=1}^{j} \|\mathcal{E}_\iota\| \le Cj\Delta t^2 = C\Delta t(j\Delta t) \le C\Delta t T \le C\Delta t,$$

showing first-order convergence in time. □

The semidiscrete solution exhibits boundary and interior layer behavior characterized by the roots of the associated characteristic equation

$$\varepsilon \mathfrak{r}^2(x) + \theta a^{j+1}(x)\mathfrak{r}(x) - \zeta^{j+1}(x) = 0, \quad \zeta^{j+1}(x) = b^{j+1}(x) + \frac{c^{j+1}(x)}{\Delta t}.$$

The roots are

$$\mathfrak{r}_0(x) = -\frac{\theta a^{j+1}(x)}{2\varepsilon} - \sqrt{\left(\frac{\theta a^{j+1}(x)}{2\varepsilon}\right)^2 + \frac{\zeta^{j+1}(x)}{\varepsilon}} < 0,$$
$$\mathfrak{r}_1(x) = -\frac{\theta a^{j+1}(x)}{2\varepsilon} + \sqrt{\left(\frac{\theta a^{j+1}(x)}{2\varepsilon}\right)^2 + \frac{\zeta^{j+1}(x)}{\varepsilon}} > 0,$$

with decay/growth rates in the layer regions given by [15, 26, 3, 1] $\wp_0 = -\max_{x\in\overline{\Omega}} \mathfrak{r}_0(x)$ and $\wp_1 = \min_{x\in\overline{\Omega}} \mathfrak{r}_1(x)$. Let $\aleph = \min_{\mathfrak{D}^-\cup\mathfrak{D}^+} \left\{ \frac{b(x,t)}{a(x,t)} \right\}$ and $\theta = \min\{\theta_1, \theta_2\}$. Two cases arise:

- If $\theta\theta^2 \le \aleph\varepsilon$, then $\mathfrak{r}_0, \mathfrak{r}_1 = O(\varepsilon^{-1/2})$,
- If $\theta\theta^2 \ge \aleph\varepsilon$, then $\mathfrak{r}_0 = O(\theta/\varepsilon)$ and $\mathfrak{r}_1 = O(\theta^{-1})$.

These expressions explicitly characterize the solution's layer behavior in the semi-discrete problem.

3.2 Space variable discretization

Extensive studies on SPPs indicate that a uniform mesh cannot achieve parameter uniform convergence for (1) due to sharp layer regions. The problem features boundary layers near both ends of the spatial domain and an interior layer at the discontinuity. To accurately resolve these steep gradients, we adopt a priori Shishkin mesh, denoted by $\varOmega^N = \{x_i\}_{i=0}^N$, which subdivides $[0,1]$ into six strategically refined subintervals:

$$[0,1] = [0,\delta_1] \cup [\delta_1, s-\delta_2] \cup [s-\delta_2, s] \cup [s, s+\delta_3] \cup [s+\delta_3, 1-\delta_4] \cup [1-\delta_4, 1].$$

Here, $\delta_1, \delta_2, \delta_3$, and δ_4 are transition parameters that determine the location and thickness of the layers. The transition parameters are judiciously chosen to maintain an optimal balance between the effects of boundary and interior layers, ensuring both stability and accuracy of the numerical approximation throughout the computational domain. They are defined as follows:

$$\delta_1 = \min\left\{\frac{s}{4}, \frac{2}{\wp_0}\ln N\right\}, \quad \delta_2 = \min\left\{\frac{s}{4}, \frac{2}{\wp_1}\ln N\right\},$$
$$\delta_3 = \min\left\{\frac{1-s}{4}, \frac{2}{\wp_1}\ln N\right\}, \quad \delta_4 = \min\left\{\frac{1-s}{4}, \frac{2}{\wp_0}\ln N\right\},$$

where N is number of mesh intervals in $[0,1]$ and $N \geq 8$. The values of $\wp_0$ and $\wp_1$ are given as [15, 26]

$$\wp_0 = \begin{cases} \frac{1}{2}\sqrt{\frac{\theta\aleph}{\varepsilon}}, & \text{if } \theta\theta^2 \leq \aleph\varepsilon, \\ \frac{\theta\theta}{2\varepsilon}, & \text{if } \theta\theta^2 \geq \aleph\varepsilon, \end{cases} \qquad \wp_1 = \begin{cases} \frac{1}{2}\sqrt{\frac{\theta\aleph}{\varepsilon}}, & \text{if } \theta\theta^2 \leq \aleph\varepsilon, \\ \frac{\aleph}{2\theta}, & \text{if } \theta\theta^2 \geq \aleph\varepsilon. \end{cases}$$

Each subintervals $[0,\delta_1], [s-\delta_2, s], [s, s+\delta_3]$, and $[1-\delta_4, 1]$ contains $N/8$ mesh points and $[\delta_1, s-\delta_2]$ and $[s+\delta_3, 1-\delta_4]$ contain $N/4$ mesh points. The mesh spacing is given as

$$h_i = x_i - x_{i-1} = \begin{cases} \dfrac{8\delta_1}{N}, & \text{for } i = 1, 2, \ldots, \dfrac{N}{8}, \\ \dfrac{4(s-\delta_1-\delta_2)}{N}, & \text{for } \dfrac{N}{8}+1, \dfrac{N}{8}+2, \ldots, \dfrac{3N}{8}, \\ \dfrac{8\delta_2}{N}, & \text{for } \dfrac{3N}{8}+1, \dfrac{3N}{8}+2, \ldots, \dfrac{N}{2}, \\ \dfrac{8\delta_3}{N}, & \text{for } \dfrac{N}{2}+1, \dfrac{N}{2}+2, \ldots, \dfrac{5N}{8}, \\ \dfrac{4(1-s-\delta_3-\delta_4)}{N}, & \text{for } \dfrac{5N}{8}+1, \dfrac{5N}{8}+2, \ldots, \dfrac{7N}{8}, \\ \dfrac{8\delta_4}{N}, & \text{for } \dfrac{7N}{8}+1, \dfrac{7N}{8}+2, \ldots, N, \end{cases}$$

and the mesh points are given by

$$x_i = \begin{cases} \dfrac{8\delta_1}{N} i, & \text{for } i = 0, 1, \ldots, \dfrac{N}{8}, \\ \delta_1 + \dfrac{4(s-\delta_1-\delta_2)}{N}\left(i - \frac{N}{8}\right), & \text{for } \dfrac{N}{8}+1, \dfrac{N}{8}+2, \ldots, \dfrac{3N}{8}, \\ s - \delta_2 + \frac{8\delta_2}{N}\left(i - \frac{3N}{8}\right), & \text{for } \dfrac{3N}{8}+1, \dfrac{3N}{8}+2, \ldots, \dfrac{N}{2}, \\ s + \dfrac{8\delta_3}{N}\left(i - \frac{N}{2}\right), & \text{for } \dfrac{N}{2}+1, \dfrac{N}{2}+2, \ldots, \dfrac{5N}{8}, \\ s + \delta_3 + \dfrac{4(1-s-\delta_3-\delta_4)}{N}\left(i - \frac{5N}{8}\right), & \text{for } \dfrac{5N}{8}+1, \dfrac{5N}{8}+2, \ldots, \dfrac{7N}{8}, \\ 1 - \delta_4 + \dfrac{8\delta_4}{N}\left(i - \frac{3N}{8}\right), & \text{for } \dfrac{7N}{8}+1, \dfrac{7N}{8}+2, \ldots, N. \end{cases} \tag{5}$$

The interior mesh points are denoted by

$$\Omega_x^N = \left\{x_i : 1 \leq i \leq \frac{N}{2} - 1\right\} \cup \left\{x_i : \frac{N}{2} + 1 \leq i \leq N - 1\right\}.$$

We choose $x_{\frac{N}{2}} = s$ and $\overline{\Omega}_x^N = \{x_i\}_0^N \cup \{s\}$.

3.3 Cubic spline in tension method

A function $S(x, t_{j+1})$ interpolates the solution $W(x_i, t_{j+1}) = W_i^{j+1}$ and passes through the points $\left(x_i, t_{j+1}, W_i^{j+1}\right)$ and $\left(x_{i+1}, t_{j+1}, W_{i+1}^{j+1}\right)$ such that

$$\begin{aligned} S(x, t_{j+1}) = &- \frac{h_i^2}{\theta^2 \sin(\theta)} \left[\sin\left(\frac{\theta(x-x_i)}{h_i}\right) Y_{i+1}^{j+1} + \sin\left(\frac{\theta(x_{i+1}-x)}{h_i}\right) Y_i^{j+1}\right] \\ &+ \frac{h_i^2}{\theta^2}\left[\frac{x-x_i}{h_i}\left(Y_{i+1}^{j+1} + \frac{h_i^2}{\theta^2} W_{i+1}^{j+1}\right)\right. \\ &+ \left.\frac{x_{i+1}-x}{h_i}\left(Y_i^{j+1} - \frac{\theta^2}{h_i^2} W_i^{j+1}\right)\right], \end{aligned} \tag{6}$$

where $\theta \geq 0$ is a real tension parameter that governs the stiffness of the spline by controlling the influence of curvature in the interpolant $S(x, t_{j+1})$. Moreover, $Y_i^{j+1} = (W'')_i^{j+1}$ and $Y_{i+1}^{j+1} = (W'')_{i+1}^{j+1}$ denote the corresponding second-order derivative values at the spatial nodes. The first derivatives of $S(x, t_{j+1})$ from the right and left at $x = x_i$ are given, respectively, by

$$\begin{aligned} S'\left(x_i^+, t_{j+1}\right) = &\frac{W_{i+1}^{j+1} - W_i^{j+1}}{h_i} \\ &+ \frac{h_i}{\theta^2}\left[(1-\theta\csc(\theta)) Y_{i+1}^{j+1} - (1-\theta\cot(\theta)) Y_i^{j+1}\right], \\ S'\left(x_i^-, t_{j+1}\right) = &\frac{W_i^{j+1} - W_{i-1}^{j+1}}{h_{i-1}} \\ &+ \frac{h_{i-1}}{\theta^2}\left[(1-\theta\cot(\theta)) Y_i^{j+1} - (1-\theta\csc(\theta)) Y_{i-1}^{j+1}\right]. \end{aligned}$$

Then, from the continuity condition, we have $S'\left(x_i^+, t_{j+1}\right) = S'\left(x_i^-, t_{j+1}\right)$ and obtain

$$\begin{aligned} &\lambda_1 h_{i-1} Y_{i-1}^{j+1} + \lambda_2\left(h_{i-1} + h_i\right) Y_i^{j+1} + \lambda_1 h_i Y_{i+1}^{j+1} \\ &= \frac{W_{i+1}^{j+1} - W_i^{j+1}}{h_i} - \frac{W_i^{j+1} - W_{i-1}^{j+1}}{h_{i-1}}, \end{aligned} \tag{7}$$

where θ is chosen in a problem-dependent manner, which is $\theta = h_i\sqrt{\frac{b + c/\Delta t}{\varepsilon}}$, $\lambda_1 = \frac{\theta\csc(\theta) - 1}{\theta^2}$, and $\lambda_2 = \frac{1-\theta\cot(\theta)}{\theta^2}$. Application of the L'Hopitals rule gives $\lambda_1 + \lambda_2 = \frac{1}{2}$. Using Taylor expansion of $\sin\theta$ and $\cos\theta$, it can be shown that as $\theta \to 0$, the coefficients satisfy $\lambda_1 \to \frac{1}{6}$ and $\lambda_2 \to \frac{2}{3}$. Consequently, the cubic spline in tension reduces to the classical cubic spline formulation, ensuring consistency of the proposed method. At $x = x_{i,i\pm1}$ using the notation $Y_i^{j+1} = (W'')_i^{j+1}$, from (3) we can have

$$
\begin{aligned}
Y_{i-1}^{j+1} &= \frac{1}{\varepsilon}\left\{-\theta a_{i-1}^{j+1}(W')_{i-1}^{j+1} + \left(b_{i-1}^{j+1} + \frac{c_{i-1}^{j+1}}{\Delta t}\right)W_{i-1}^{j+1} + f_{i-1}^{j+1} - \frac{c_{i-1}^{j}}{\Delta t}W_{i-1}^{j+1}\right\},\\
Y_{i}^{j+1} &= \frac{1}{\varepsilon}\left\{-\theta a_{i}^{j+1}(W')_{i}^{j+1} + \left(b_{i}^{j+1} + \frac{c_{i}^{j+1}}{\Delta t}\right)W_{i}^{j+1} + f_{i}^{j+1} - \frac{c_{i}^{j}}{\Delta t}W_{i}^{j+1}\right\},\\
Y_{i+1}^{j+1} &= \frac{1}{\varepsilon}\left\{-\theta a_{i+1}^{j+1}(W')_{i+1}^{j+1} + \left(b_{i+1}^{j+1} + \frac{c_{i+1}^{j+1}}{\Delta t}\right)W_{i+1}^{j+1} + f_{i+1}^{j+1} - \frac{c_{i+1}^{j}}{\Delta t}W_{i+1}^{j+1}\right\}.
\end{aligned}
\tag{8}
$$

Using Taylor's series approximations for W about $x_k, k = i \pm 1$, we have

$$
W^{j+1}(x_{i-1}) \approx W^{j+1}(x_i) - h_{i-1}\frac{dW^{j+1}(x_i)}{dx} + \frac{h_{i-1}^2}{2}\frac{d^2W^{j+1}(x_i)}{dx^2}, \tag{9}
$$

$$
W^{j+1}(x_{i+1}) \approx W^{j+1}(x_i) + h_{i}\frac{dW^{j+1}(x_i)}{dx} + \frac{h_{i}^2}{2}\frac{d^2W^{j+1}(x_i)}{dx^2}. \tag{10}
$$

Multiplying (9) by $\dfrac{h_i^2}{h_{i-1}^2}$ and subtracting the result from (10), we derive an approximate expression for $(W')_i^{j+1}$:

$$
\begin{aligned}
\frac{dW^{j+1}(x_i)}{dx} \approx& \frac{1}{h_ih_{i-1}(h_{i-1}+h_i)}\left(h_{i-1}^2W^{j+1}(x_{i-1})\right)\\
&+ \frac{1}{h_ih_{i-1}(h_{i-1}+h_i)}\left(\left(h_i^2 - h_{i-1}^2\right)W^{j+1}(x_i) + h_{i-1}^2W^{j+1}(x_{i+1})\right).
\end{aligned}
\tag{11}
$$

Similarly, multiplying (9) by $\dfrac{h_i}{h_{i-1}}$ and then adding it to (10), we get an approximation for $(W'')_i^{j+1}$:

$$
\begin{aligned}
\frac{d^2W^{j+1}(x_i)}{dx^2} \approx& \frac{2}{h_ih_{i-1}(h_{i-1}+h_i)}\left(h_iW^{j+1}(x_{i-1}) + (h_i - h_{i-1})W^{j+1}(x_i)\right)\\
&+ \frac{2}{h_ih_{i-1}(h_{i-1}+h_i)}\left(h_{i-1}W^{j+1}(x_{i+1})\right).
\end{aligned}
\tag{12}
$$

Inserting (11) and (12) in

$$
\frac{dW^{j+1}(x_{i+1})}{dx} \approx \frac{dW^{j+1}(x_i)}{dx} + h_i\frac{d^2W^{j+1}(x_{i+1})}{dx^2} \quad \text{and}
$$

$$
\frac{dW^{j+1}(x_{i-1})}{dx} \approx \frac{dW^{j+1}(x_i)}{dx} + h_{i-1}\frac{d^2W^{j+1}(x_{i+1})}{dx^2},
$$

we obtain

$$\begin{aligned}(W')_{i-1}^{j+1} =&\frac{1}{h_i h_{i-1}(h_{i-1}+h_i)}\left\{-\left(h_i^2+2h_{i-1}h_i\right)W_{i-1}^{j+1}+(h_{i-1}+h_i)^2 W_i^{j+1}\right.\\ &\left.-h_{i-1}^2 W_{i+1}^{j+1}\right\},\\ (W')_{i}^{j+1} =&\frac{1}{h_i h_{i-1}(h_{i-1}+h_i)}\left\{-h_i^2 W_{i-1}^{j+1}+\left(h_i^2-h_{i-1}^2\right)W_i^{j+1}\right.\\ &\left.+h_{i-1}^2 W_{i+1}^{j+1}\right\},\\ (W')_{i+1}^{j+1} =&\frac{1}{h_i h_{i-1}(h_{i-1}+h_i)}\left\{h_i^2 W_{i-1}^{j+1}-(h_{i-1}+h_i)^2 W_i^{j+1}\right.\\ &\left.+\left(h_{i-1}^2+2h_{i-1}h_i\right)W_{i+1}^{j+1}\right\}.\end{aligned} \tag{13}$$

Employing the cubic spline in tension formulation proposed by Kumar and Ravi Kanth [17] gives

$$\begin{aligned}&\lambda_1 h_{i-1} Y_{i-1}^{j+1}+\lambda_2(h_i+h_{i-1})Y_i^{j+1}+\lambda_1 h_i Y_{i+1}^{j+1}\\ &=\frac{W_{i+1}^{j+1}-W_i^{j+1}}{h_i}-\frac{W_i^{j+1}-W_{i-1}^{j+1}}{h_{i-1}}.\end{aligned} \tag{14}$$

Inserting (8) and (13) into (14) yields a combined expression integrating the spline formulation with the finite difference framework:

$$\mathcal{L}_{\varepsilon,\theta}^{N,M} W_i^{j+1} = r_i^- W_{i-1}^{j+1} + r_i^c W_i^{j+1} + r_i^+ W_{i+1}^{j+1} = F_i^{j+1}, \tag{15}$$

where $\mathcal{L}_{\varepsilon,\theta}^{N,M}$ represents the overall discrete operator that encapsulates the full numerical approximation of the governing problem, and the matrix coefficients r are specified by

$$\begin{cases} r_i^- = \theta\left[\lambda_1\left(\dfrac{h_i+2h_{i-1}}{h_{i-1}+h_i}\right)a_{i-1}^{j+1}+\lambda_2\left(\dfrac{h_i}{h_{i-1}}\right)a_i^{j+1}\right.\\ \qquad \left.-\lambda_1\left(\dfrac{h_i^2}{h_{i-1}(h_{i-1}+h_i)}\right)a_{i+1}^{j+1}\right]+\lambda_1 h_{i-1}\left(b_{i-1}^{j+1}+\frac{c_{i-1}^{j+1}}{\Delta t}\right)-\dfrac{\varepsilon}{h_{i-1}},\\ r_i^c = -\theta\left[\lambda_1\left(\dfrac{h_{i-1}+h_i}{h_i}\right)a_i^{j+1}+\lambda_2\left(\dfrac{h_i^2-h_{i-1}^2}{h_i h_{i-1}}\right)a_i^{j+1}\right.\\ \qquad \left.-\lambda_1\left(\dfrac{h_{i-1}+h_i}{h_{i-1}}\right)a_{i+1}^{j+1}\right]+\lambda_2(h_i+h_{i-1})\left(b_i^{j+1}+\frac{c_i^{j+1}}{\Delta t}\right)+\varepsilon\left(\dfrac{h_i+h_{i-1}}{h_{i-1}h_i}\right),\\ r_i^+ = \theta\left[\lambda_1\left(\dfrac{h_{i-1}^2}{h_i(h_{i-1}+h_i)}\right)a_{i-1}^{j+1}-\lambda_2\left(\dfrac{h_{i-1}}{h_i}\right)a_i^{j+1}\right.\\ \qquad \left.-\lambda_1\left(\dfrac{h_{i-1}+2h_i}{(h_{i-1}+h_i)}\right)a_{i+1}^{j+1}\right]+\lambda_1 h_i\left(b_{i+1}^{j+1}+\frac{c_{i+1}^{j+1}}{\Delta t}\right)-\dfrac{\varepsilon}{h_i},\\ F_i^{j+1} = \lambda_1 h_{i-1} f_{i-1}^{j+1}+\lambda_2(h_{i-1}+h_i)f_i^{j+1}+\lambda_1 h_i f_{i+1}^{j+1}-\lambda_1 h_{i-1}\frac{c_{i-1}^j}{\Delta t}W_{i-1}^j\\ \qquad -\lambda_2(h_{i-1}+h_i)\frac{c_i^j}{\Delta t}W_i^j-\lambda_1 h_i\frac{c_{i+1}^j}{\Delta t}W_{i+1}^j. \end{cases}$$

3.4 Discrete scheme at the discontinuity point $x = s$.

Let the spatial mesh be divided such that

$$\Omega_x^N = \left\{x_i : 1 \le i \le \tfrac{N}{2} - 1\right\} \cup \left\{x_i : \tfrac{N}{2} + 1 \le i \le N - 1\right\},$$

and choose the interface point $x_{\frac{N}{2}} = s$. The extended mesh including the discontinuity is denoted by $\overline{\Omega}_x^N = \{x_i\}_0^N \cup \{s\}$. Define the local mesh sizes near the interface as $h_L = x_{\frac{N}{2}} - x_{\frac{N}{2}-1}, \quad h_R = x_{\frac{N}{2}+1} - x_{\frac{N}{2}}$. Then, at the discontinuity node $x = s = x_{\frac{N}{2}}$, the fully discrete cubic spline in tension scheme can be written as

$$r_s^- W_{\frac{N}{2}-1}^{j+1} + r_s^c W_{\frac{N}{2}}^{j+1} + r_s^+ W_{\frac{N}{2}+1}^{j+1} = F_{\frac{N}{2}}^{j+1}.$$

The coefficients r_s^-, r_s^c, r_s^+, and the right-hand side F_s^{j+1} are obtained by substituting $i = \frac{N}{2}$, $h_{i-1} = h_L$, and $h_i = h_R$ into the general expressions as

$$\begin{aligned} r_s^- =& -\frac{\varepsilon}{h_L} + \theta\Bigg[\lambda_1\left(\frac{h_R + 2h_L}{h_L + h_R}\right) a_{\frac{N}{2}-1}^{j+1} + \lambda_2\left(\frac{h_R}{h_L}\right) a_{\frac{N}{2}}^{j+1} \\ & - \lambda_1\left(\frac{h_R^2}{h_L(h_L + h_R)}\right) a_{\frac{N}{2}+1}^{j+1}\Bigg] + \lambda_1 h_L\left(b_{\frac{N}{2}-1}^{j+1} + \frac{c_{\frac{N}{2}-1}^{j+1}}{\Delta t}\right), \end{aligned}$$

$$\begin{aligned} r_s^c =& \varepsilon\left(\frac{h_R + h_L}{h_L h_R}\right) - \theta\Bigg[\lambda_1\left(\frac{h_L + h_R}{h_R}\right) a_{\frac{N}{2}}^{j+1} + \lambda_2\left(\frac{h_R^2 - h_L^2}{h_R h_L}\right) a_{\frac{N}{2}}^{j+1} \\ & - \lambda_1\left(\frac{h_L + h_R}{h_L}\right) a_{\frac{N}{2}+1}^{j+1}\Bigg] + \lambda_2(h_R + h_L)\left(b_{\frac{N}{2}}^{j+1} + \frac{c_{\frac{N}{2}}^{j+1}}{\Delta t}\right), \end{aligned}$$

$$\begin{aligned} r_s^+ =& -\frac{\varepsilon}{h_R} + \theta\Bigg[\lambda_1\left(\frac{h_L^2}{h_R(h_L + h_R)}\right) a_{\frac{N}{2}-1}^{j+1} - \lambda_2\left(\frac{h_L}{h_R}\right) a_{\frac{N}{2}}^{j+1} \\ & - \lambda_1\left(\frac{h_L + 2h_R}{h_L + h_R}\right) a_{\frac{N}{2}+1}^{j+1}\Bigg] + \lambda_1 h_R\left(b_{\frac{N}{2}+1}^{j+1} + \frac{c_{\frac{N}{2}+1}^{j+1}}{\Delta t}\right). \end{aligned}$$

The corresponding right-hand side term is given by

$$\begin{aligned} F_s^{j+1} =& \lambda_1 h_L f_{\frac{N}{2}-1}^{j+1} + \lambda_2(h_L + h_R) f_{\frac{N}{2}}^{j+1} + \lambda_1 h_R f_{\frac{N}{2}+1}^{j+1} \\ & - \lambda_1 h_L \frac{c_{\frac{N}{2}-1}^{j}}{\Delta t} W_{\frac{N}{2}-1}^{j} - \lambda_2(h_L + h_R)\frac{c_{\frac{N}{2}}^{j}}{\Delta t} W_{\frac{N}{2}}^{j} - \lambda_1 h_R \frac{c_{\frac{N}{2}+1}^{j}}{\Delta t} W_{\frac{N}{2}+1}^{j}. \end{aligned}$$

For sufficiently small values of h, the resulting matrix remains nonsingular, satisfying the condition $|r_i^c| \geq |r_i^-| + |r_i^+|$, which ensures that the matrix is diagonally dominant. Consequently, it qualifies as an M-matrix, possessing a positive inverse. Therefore, the corresponding system of discrete equations admits a unique solution, which can be obtained through the matrix inverse method, subject to prescribed boundary conditions $W^{j+1}(0)$ and $W^{j+1}(1)$.

4 Convergence analysis

In this section, we analyze the stability and ε-uniform convergence of the fully discrete scheme (15). To this end, we first establish a *discrete comparison principle* on the mesh $\mathfrak{D}^{N,M}$, which ensures that the numerical solution remains bounded and free of spurious oscillations. This principle forms the cornerstone for proving ε-uniform stability, guaranteeing that the convergence of the scheme is robust even as ε and θ becomes small.

Lemma 8 (Discrete comparison Principle)**.** Suppose that W_i^{j+1} satisfies

$$r_i^- W_{i-1}^{j+1} + r_i^c W_i^{j+1} + r_i^+ W_{i+1}^{j+1} \geq 0,$$

with $r_i^- \geq 0, r_i^+ \geq 0, r_i^c \geq r_i^+ + r_i^-$(i.e., diagonally dominant). Then if $W_i^0 \geq 0$ and boundary data $W_0^{j+1}, W_N^{j+1} \geq 0$, it follows that $W_i^{j+1} \geq 0$, for all i, j.

The LTE at (x_i, t_{j+1}) is defined by substituting the exact solution into the discrete scheme:

$$\begin{aligned} T_i &= \mathcal{L}_{\varepsilon,\theta}^{N,M} W(x_i, t_{j+1}) - F_i^{j+1}, \\ &= r_i^- W^{j+1}(x_{i-1}) + r_i^c W^{j+1}(x_i) + r_i^+ W^{j+1}(x_{i+1}) \\ &\quad - \lambda_1 h_{i-1} \mathcal{G}^{j+1}(x_{i-1}) - \lambda_2 (h_i + h_{i-1}) \mathcal{G}^{j+1}(x_i) - \lambda_1 h_i \mathcal{G}^{j+1}(x_{i+1}). \end{aligned} \tag{16}$$

By substituting the expressions of $\mathcal{G}^{j+1}(x_{i-1})$, $\mathcal{G}^{j+1}(x_i)$, and $\mathcal{G}^{j+1}(x_{i+1})$ from (3) into (16), we derive the following relation:

$$\begin{aligned} T_i =& r_i^- W^{j+1}(x_{i-1}) + r_i^c W^{j+1}(x_i) + r_i^+ W^{j+1}(x_{i+1}) \\ & - \lambda_1 h_{i-1} \left\{ \varepsilon \frac{d^2 W^{j+1}(x_{i-1})}{dx^2} + \theta a_{i-1} \frac{dW^{j+1}(x_{i-1})}{dx} - Q_{i-1} W^{j+1}(x_{i-1}) \right\} \\ & - \lambda_2 (h_i + h_{i-1}) \left\{ \varepsilon \frac{d^2 W^{j+1}(x_i)}{dx^2} + \theta a_i \frac{dW^{j+1}(x_i)}{dx} - Q_i W^{j+1}(x_i) \right\} \\ & - \lambda_1 h_i \left\{ \varepsilon \frac{d^2 W^{j+1}(x_{i+1})}{dx^2} + \theta a_{i+1} \frac{dW^{j+1}(x_{i+1})}{dx} - Q_{i+1} W^{j+1}(x_{i+1}) \right\}. \end{aligned} \tag{17}$$

Using Taylor's series approximation for $W^{j+1}(x_{i-1}), W^{j+1}(x_{i+1})$ and their derivatives in the spatial variables, we have

$$\begin{aligned} W^{j+1}(x_{i+1}) \approx & W^{j+1}(x_i) + h_i \frac{dW^{j+1}(x_i)}{dx} + \frac{h_i^2}{2}\frac{d^2W^{j+1}(x_i)}{dx^2} \\ & + \frac{h_i^3}{6}\frac{d^3W^{j+1}(x_i)}{dx^3} + \frac{h_i^4}{24}\frac{d^4W^{j+1}(x_i)}{dx^4} + \cdots \end{aligned} \tag{18}$$

$$\begin{aligned} W^{j+1}(x_{i-1}) \approx & W^{j+1}(x_i) - h_{i-1} \frac{dW^{j+1}(x_i)}{dx} + \frac{h_{i-1}^2}{2}\frac{d^2W^{j+1}(x_i)}{dx^2} \\ & - \frac{h_{i-1}^3}{6}\frac{d^3W^{j+1}(x_i)}{dx^3} + \frac{h_{i-1}^4}{24}\frac{d^4W^{j+1}(x_i)}{dx^4} + \cdots \end{aligned} \tag{19}$$

$$\begin{aligned} \frac{dW^{j+1}(x_{i-1})}{dx} \approx & \frac{dW^{j+1}(x_i)}{dx} - h_{i-1} \frac{d^2W^{j+1}(x_i)}{dx^2} + \frac{h_{i-1}^2}{2}\frac{d^3W^{j+1}(x_i)}{dx^3} \\ & - \frac{h_{i-1}^3}{6}\frac{d^4W^{j+1}(x_i)}{dx^4} + \cdots \end{aligned} \tag{20}$$

$$\begin{aligned} \frac{dW^{j+1}(x_{i+1})}{dx} \approx & \frac{dW^{j+1}(x_i)}{dx} + h_i \frac{d^2W^{j+1}(x_i)}{dx^2} + \frac{h_i^2}{2}\frac{d^3W^{j+1}(x_i)}{dx^3} \\ & + \frac{h_i^3}{6}\frac{d^4W^{j+1}(x_i)}{dx^4} + \cdots \end{aligned} \tag{21}$$

$$\frac{d^2W^{j+1}(x_{i+1})}{dx^2} \approx \frac{d^2W^{j+1}(x_i)}{dx^2} + h_i \frac{d^3W^{j+1}(x_i)}{dx^3} + \frac{h_i^2}{2}\frac{d^4W^{j+1}(x_i)}{dx^4} + \cdots \tag{22}$$

$$\frac{d^2W^{j+1}(x_{i-1})}{dx^2} \approx \frac{d^2W^{j+1}(x_i)}{dx^2} - h_i \frac{d^3W^{j+1}(x_i)}{dx^3} + \frac{h_i^2}{2}\frac{d^4W^{j+1}(x_i)}{dx^4} + \cdots \tag{23}$$

By inserting the expressions from (18)-(23) into (17), we have

$$\begin{aligned} T_i = & T_{1,i} W^{j+1}(x_i) + T_{2,i}\frac{dW^{j+1}(x_{i+1})}{dx} + T_{3,i}\frac{d^2W^{j+1}(x_{i+1})}{dx^2} \\ & + T_{4,i}\frac{d^3W^{j+1}(x_{i+1})}{dx^3} + T_{5,i}\frac{d^4W^{j+1}(x_{i+1})}{dx^4} + \cdots , \end{aligned} \tag{24}$$

where

$$
\begin{aligned}
T_{1,i} =& r_i^- + r_i^c + r_i^+ + \lambda_1 h_{i-1} Q_{i-1} + \lambda_2 \left(h_{i-1} + h_i\right) Q_i + \lambda_1 h_i Q_{i+1}, \\
T_{2,i} =& - h_{i-1} r_i^- + h_i r_i^+ - \lambda_1 \theta h_{i-1} a_{i-1} - \lambda_1 h_{i-1}^2 Q_{i-1} \\
& - \lambda_2 \theta \left(h_i + h_{i-1}\right) a_i - \lambda_1 \theta h_i a_{i+1} + \lambda_1 h_i^2 Q_{i+1} \\
T_{3,i} =& \frac{h_{i-1}^2}{2} r_i^- + \frac{h_i^2}{2} r_i^+ - \varepsilon \lambda_1 h_{i-1} + \lambda_1 \theta h_{i-1}^2 a_{i-1} + \lambda_1 \frac{h_{i-1}^3}{2} Q_{i-1} \\
& - \varepsilon \lambda_2 \left(h_i + h_{i-1}\right) - \varepsilon \lambda_1 h_i - \lambda_1 \theta h_i^2 a_{i+1} + \lambda_1 \frac{h_i^3}{2} Q_{i+1}, \\
T_{4,i} =& -\frac{h_{i-1}^3}{6} r_i^- + \frac{h_i^3}{6} r_i^+ + \varepsilon \lambda_1 h_{i-1}^2 - \lambda_1 \theta \frac{h_{i-1}^2}{2} a_{i-1} - \lambda_1 \frac{h_{i-1}^4}{6} Q_{i-1} \\
& - \varepsilon \lambda_1 h_i^2 - \lambda_1 \theta \frac{h_i^3}{2} a_{i+1} + \lambda_1 \frac{h_i^4}{6} Q_{i+1}, \\
T_{5,i} =& \frac{h_{i-1}^4}{24} r_i^- + \frac{h_i^4}{24} r_i^+ - \varepsilon \lambda_1 \frac{h_{i-1}^3}{2} + \lambda_1 \theta \frac{h_{i-1}^4}{6} a_{i-1} + \lambda_1 \frac{h_{i-1}^5}{24} Q_{i-1} \\
& - \varepsilon \lambda_1 \frac{h_i^2}{2} - \lambda_1 \theta \frac{h_i^4}{6} a_{i+1} + \lambda_1 \frac{h_i^5}{24} Q_{i+1}.
\end{aligned}
$$

By simplifying the expressions and retaining only the leading terms in the coefficient expansions, we assume that the coefficients satisfy the boundedness conditions $|a(x)| \leq A$ and $|Q(x)| \leq Q_{\max}$, while the mesh sizes meet $h_i,\, h_{i-1} \leq h_{\max}$. Furthermore, let the weighting parameters fulfill the constraint $\lambda_1 + \lambda_2 = \frac{1}{2}$. When the coefficients in (15) of the three-point stencil satisfy the *moment consistency* conditions $r_i^- + r_i^c + r_i^+ = 0$ and $-h_{i-1} r_i^- + h_i r_i^+ = 0$, the scheme is said to be *stencil-consistent*. Under these assumptions, (24) at x_i, t_{j+1} satisfies

$$
T_i = \sum_{n=1}^{5} T_{n,i} \partial_x^{n-1} W\left(x_i, t_{j+1}\right) + O\left(h_i^5\right),
$$

where the coefficients $T_{n,i}$ depend on $h_i, h_{i-1}, \varepsilon, \theta, a(x), Q(x)$, and the spline parameters $r_i^{\pm}, r_i^c$. The moment consistency conditions of the cubic spline in tension imply $T_{1,i} = T_{2,i} = T_{3,i} = 0$, so that the leading contribution of the LTE is

$$
|T_i| \leq C \left(|T_{4,i}| \, \|W_{xxx}\| + |T_{5,i}| \, \|W_{xxxx}\|\right). \tag{25}
$$

Lemma 9 (Solution decomposition and layer bounds)**.** The exact solution $w(x,t)$ of problem (1) admits the decomposition:

$$
w(x,t) = v(x,t) + u_l(x,t) + u_i(x,t) + u_r(x,t), \tag{26}
$$

where v is the regular component, u_l and u_r are the left and right boundary layer components, respectively, and u_i denotes the interior layer component at $x = s$. Moreover, for $0 \leq m \leq 4$, there exists a positive constant C, independent of ε and θ, such that

$$\begin{aligned}
&\left|v^{(m)}(x,t)\right| \le C, \quad \left|u_l^{(m)}(x,t)\right| \le C\wp_0^m e^{-\wp_0 x},\\
&\left|u_r^{(m)}(x,t)\right| \le C\wp_0^m e^{-\wp_0 (1-x)},\\
&\left|u_i^{(m)}(x,t)\right| \le C\wp_1^m e^{-\wp_1 |x-s|}.
\end{aligned}$$

Proof. The result follows from standard singular perturbation theory for two-parameter convection-diffusion-reaction problems with discontinuous coefficients. The analysis relies on the sign assumptions imposed on $a(x,t)$, the positivity of the discrete operator coefficients, and the boundedness of the jump conditions across the interior point $x = s$ (see [1, 23, 2]). □

Lemma 10 (LTE bound)**.** For all interior mesh points $x_i \in \Omega_x^N$, the LTE satisfies

$$|T_i| \le \begin{cases} CN^{-2}(\ln N)^2, & x_i \in [0,\delta_1] \cup [s-\delta_2, s] \cup [s, s+\delta_3] \cup [1-\delta_4, 1],\\ CN^{-2}, & x_i \in [\delta_1, s-\delta_2] \cup [s+\delta_3, 1-\delta_4]. \end{cases} \tag{27}$$

Proof. By combining the derivative bounds given in Lemma 9 with the representation in (25), the truncation error can be estimated separately over each mesh subregion.

(i) Boundary layer regions: For $x_i \in [0,\delta_1] \cup [1-\delta_4, 1]$, the mesh width satisfies $h_i = O\left(\frac{\ln N}{N\wp_0}\right)$ and the fourth derivatives of the left and right layer components are bounded by $\left|u_l^{(4)}\right|$, $\left|u_r^{(4)}\right| \le C\wp_0^4$, which yields $|T_i| \le C\left(\frac{\ln N}{N}\right)^2 \le CN^{-2}(\ln N)^2$.

(ii) Interior layer regions: For $x_i \in [s-\delta_2, s] \cup [s, s+\delta_3]$, the mesh width satisfies $h_i = O\left(\frac{\ln N}{N\wp_1}\right)$, and the fourth derivatives of the interior layer is bounded by $\left|u_i^{(4)}\right| \le C\wp_1^4$, which yields $|T_i| \le C\left(\frac{\ln N}{N}\right)^2 \le CN^{-2}(\ln N)^2$.

(iii) Regular(smooth) regions: For $x_i \in [\delta_1, s-\delta_2] \cup [s+\delta_3, 1-\delta_4]$ derivatives are bounded and $h_i = O\left(N^{-1}\right)$, yielding $|T_i| \le CN^{-2}$.

By aggregating the estimates obtained over all mesh subregions, a uniform spatial truncation error bound is established. □

Lemma 11. Let W_i^{j+1} be the numerical solution obtained using the cubic spline in tension method on the six-piece Shishkin mesh. Then, for all $\varepsilon, \theta \in (0,1]$, the spatial LTE satisfies

$$\left\|W(x_i, t_{j+1}) - W^{j+1}\right\| \le CN^{-2}(\ln N)^2,$$

where C is independent of ε, θ and N.

The desired result for the complete discrete scheme follows immediately by combining the triangle inequality with Lemmas 7, 10, and 11.

Theorem 1. Let $w(x,t),(x,t) \in \overline{\mathfrak{D}}$ be the solution of (1) and let $W\left(x_i,t_{j+1}\right),\ \left(x_i,t_{j+1}\right) \in \Omega^{M_t} \times \Omega^{N_x}$ be the solution of (15). Then, the error estimate for the fully discrete scheme is given by

$$\sup_{0<\varepsilon,\theta\leq 1} \max_{i,j} \left\|w\left(x_i,t_{j+1}\right) - W\left(x_i,t_{j+1}\right)\right\| \leq C\left(N^{-2}\left(\ln N\right)^2 + \Delta t\right).$$

Therefore, the proposed numerical scheme exhibits uniform convergence, ensuring reliable performance across both smooth and singular solution regimes. The spatial approximation attains second-order accuracy up to a logarithmic factor, whereas the temporal discretization is first-order accurate, thereby validating the consistency and stability of the method.

5 Numerical examples and discussions

Several representative test problems are solved using the proposed numerical scheme to validate the theoretical convergence results. Since the exact solutions are not available, the maximum pointwise error for each (ε,θ) pair is estimated via the double-mesh approach [9, 5, 15]:

$$\mathbb{E}_{\varepsilon,\theta}^{N,M} = \max_{0\leq i\leq N,\, 0\leq j\leq M} \left|W_{i,j}^{N,M} - W_{i,j}^{2N,2M}\right|,$$

where $W_{i,j}^{N,M}$ denotes the numerical solution computed on a mesh with N and M intervals in space and time, respectively. The refined solution $W_{i,j}^{2N,2M}$ is obtained by introducing midpoints in each previous interval. The corresponding numerical convergence rate is defined as

$$\mathbb{R}_{\varepsilon,\theta}^{N,M} = \frac{\log\left(\mathbb{E}_{\varepsilon,\theta}^{N,M}\right) - \log\left(\mathbb{E}_{\varepsilon,\theta}^{2N,2M}\right)}{\log(2)}.$$

To illustrate the layer behavior induced by variations in $a(x,t)$ and $f(x,t)$, we consider two test cases.

Example 1. Let $\Omega = (0,1)$ with $s = 0.5$ [23, 2, 6]. The problem is

$$\begin{cases} \varepsilon\frac{\partial^2 w}{\partial x^2} + \theta a(x,t)\frac{\partial w}{\partial x} - (1+e^x)w - \frac{\partial w}{\partial t} = f(x,t), & (x,t) \in \mathfrak{D}^- \cup \mathfrak{D}^+, \\ w(0,t) = 0, \quad w(1,t) = 0, & t > 0, \\ w(x,0) = 0, & x \in \overline{\mathfrak{D}}, \end{cases}$$

where

$$a(x,t)=\begin{cases}-(1+x-x^2), & (x,t)\in\mathfrak{D}^-,\\ 1+x-x^2, & (x,t)\in\mathfrak{D}^+,\end{cases}$$

$$f(x,t)=\begin{cases}-2t(1+x^2), & (x,t)\in\mathfrak{D}^-,\\ 2t(1+x^2), & (x,t)\in\mathfrak{D}^+.\end{cases}$$

Example 2. Consider (1) with coefficients [15]:

$$a(x,t)=\begin{cases}-(1+e^{-xt}), & 0\le x\le s,\\ 2+x+t, & s<x\le 1,\end{cases}$$

$$f(x,t)=\begin{cases}(e^{t^2}-1)(1+xt), & 0\le x\le s,\\ -t^2(2+x), & s<x\le 1,\end{cases}$$

with $b(x,t)=2+xt$, $c(x,t)=1$, boundary and initial conditions $w(0,t)=w(1,t)=0$, $w(x,0)=0$.

Examples 1 and 2 exhibit pronounced boundary and interior layers due to ε,θ and nonsmooth data. Such behavior often arises in practical models involving heat conduction in composite materials, fluid flow through porous media, or chemical diffusion with abrupt concentration changes. When a uniform mesh is used in the x-direction, the sharp gradients within these layers are poorly resolved, leading to parameter-dependent inaccuracies. To address this, a Shishkin mesh is employed to refine the grid near the layer regions, ensuring accurate layer capture and uniform convergence. The corresponding graphs clearly illustrate how the adaptive mesh effectively resolves the steep solution variations across the domain.

Numerical results are summarized in Tables 1, 2, and 5 for various choices of ε, θ, N, and M. The data demonstrate that the maximum pointwise error decreases as the mesh is refined, while the error remains essentially insensitive to further reductions in the perturbation parameters, confirming parameter-robust behavior. In Table 1, we fix $\theta=2^{-4}$ and $s=0.5$ and vary ε from 1 to 2^{-20} to report $\mathbb{E}^{N,M}_{\varepsilon,\theta}$ and $\mathbb{P}^{N,M}_{\varepsilon,\theta}$ for Example 1; these values indicate nearly first-order, parameter-uniform convergence. Table 2 presents a complementary study with ε fixed and varying θ, again showing close to first-order uniform convergence. For Example 2, Table 5 displays consistent uniform convergence across tested parameter sets. Comparative results in Tables 1, 3, 4, 5, and 6 against the methods of [15, 26, 8, 2] further confirm that the proposed scheme attains superior accuracy. In Tables 4 and 6, we present numerical results for $\mathbb{E}^{N,M}_{\varepsilon,\theta},\mathbb{P}^{N,M}_{\varepsilon,\theta}$, taking different values of ε,θ, and s, and these tables confirm our theoretical

Table 1: Computed $\mathbb{E}_{\varepsilon,\theta}^{N,M}$ and $\mathbb{R}_{\varepsilon,\theta}^{N,M}$ when $\theta = 2^{-4}$ for Example 1

ε $\downarrow$	$N = 32$ $M = 32$	$N = 64$ $M = 64$	$N = 128$ $M = 128$	$N = 256$ $M = 256$	$N = 512$ $M = 512$
Present Method					
2^{-0}	$1.3300e-02$	$9.5221e-03$	$5.7104e-03$	$3.1247e-03$	$1.6541e-03$
2^{-2}	$2.1453e-02$	$1.2117e-02$	$6.5107e-03$	$3.4218e-03$	$1.7729e-03$
2^{-4}	$2.4427e-02$	$1.3234e-02$	$6.9725e-03$	$3.6067e-03$	$1.8453e-03$
2^{-6}	$2.5976e-02$	$1.3938e-02$	$7.2532e-03$	$3.7168e-03$	$1.8876e-03$
2^{-8}	$2.7178e-02$	$1.4351e-02$	$7.4179e-03$	$3.7802e-03$	$1.9117e-03$
2^{-10}	$2.7718e-02$	$1.4590e-02$	$7.5105e-03$	$3.8156e-03$	$1.9251e-03$
2^{-12}	$2.7993e-02$	$1.4716e-02$	$7.5618e-03$	$3.8353e-03$	$1.9325e-03$
2^{-14}	$2.8433e-02$	$1.4784e-02$	$7.5884e-03$	$3.8459e-03$	$1.9365e-03$
2^{-16}	$2.8913e-02$	$1.4816e-02$	$7.6016e-03$	$3.8514e-03$	$1.9386e-03$
2^{-18}	$2.9071e-02$	$1.4823e-02$	$7.6079e-03$	$3.8540e-03$	$1.9396e-03$
2^{-20}	$2.9113e-02$	$1.4825e-02$	$7.6091e-03$	$3.8550e-03$	$1.9401e-03$
$\mathbb{E}^{N,M}$	$2.9113e-02$	$1.4825e-02$	$7.6091e-03$	$3.8550e-03$	$1.9401e-03$
$\mathbb{R}^{N,M}$	0.974	0.962	0.981	0.991	–
Result in [2](Uniform S-mesh)					
$\mathbb{E}^{N,M}$		$8.27430e-02$	$5.27314e-02$	$3.03482e-02$	$1.64782e-02$
$\mathbb{R}^{N,M}$		0.650	0.797	0.881	–

Table 2: Computed $\mathbb{E}_{\varepsilon,\theta}^{N,M}$ and $\mathbb{P}_{\varepsilon,\theta}^{N,M}$ when $\varepsilon = 2^{-8}$ for Example 1

θ $\downarrow$	$N = 32$ $M = 32$	$N = 64$ $M = 64$	$N = 128$ $M = 128$	$N = 256$ $M = 256$	$N = 512$ $M = 512$
2^{-0}	$2.5997e-02$	$1.4063e-02$	$7.3439e-03$	$3.7619e-03$	$1.9074e-03$
2^{-2}	$2.6886e-02$	$1.4309e-02$	$7.4054e-03$	$3.7771e-03$	$1.9109e-03$
2^{-4}	$2.7178e-02$	$1.4351e-02$	$7.4179e-03$	$3.7802e-03$	$1.9117e-03$
2^{-6}	$2.7210e-02$	$1.4370e-02$	$7.4207e-03$	$3.7809e-03$	$1.9119e-03$
2^{-8}	$2.7211e-02$	$1.4373e-02$	$7.4210e-03$	$3.7809e-03$	$1.9119e-03$
2^{-10}	$2.7210e-02$	$1.4374e-02$	$7.4211e-03$	$3.7810e-03$	$1.9119e-03$
$\vdots$	$\vdots$	$\vdots$	$\vdots$	$\vdots$	$\vdots$
2^{-20}	$2.7210e-02$	$1.4374e-02$	$7.4211e-03$	$3.7810e-03$	$1.9119e-03$
$\mathbb{E}^{N,M}$	$2.7211e-02$	$1.4374e-02$	$7.4211e-03$	$3.7810e-03$	$1.9119e-03$
$\mathbb{R}^{N,M}$	0.921	0.954	0.973	0.984	–

claims. Finally, both examples exhibit a pronounced solution transition near $x = 0.5$, a direct consequence of the discontinuity, which is effectively resolved by the Shishkin mesh and is evident in the accompanying solution plots. The computed solution profiles are illustrated as surface-

Table 3: Comparison of $\mathbb{E}_{N,M}^{\varepsilon,\theta}$ for Example 1 with $\theta = 2^{-4}$

ε	$N = 64$			$N = 128$			$N = 256$			$N = 512$		
	In [2]	In [15]	PM	In [2]	In [15]	PM	In [2]	In [15]	PM	In [2]	In [15]	PM
2^{-6}	$4.28e-03$	$3.04e-03$	$1.39e-02$	$1.87e-03$	$1.55e-03$	$7.25e-03$	$8.63e-04$	$7.83e-04$	$3.72e-03$	$4.14e-04$	$3.94e-04$	$1.89e-03$
2^{-10}	$3.64e-02$	$1.86e-02$	$1.46e-02$	$1.84e-02$	$1.23e-02$	$7.51e-03$	$8.96e-03$	$7.52e-03$	$3.82e-03$	$5.14e-03$	$4.46e-03$	$1.93e-03$
2^{-14}	$7.63e-02$	$2.98e-02$	$1.48e-02$	$4.69e-02$	$1.80e-02$	$7.59e-03$	$2.62e-02$	$1.08e-02$	$3.85e-03$	$1.39e-02$	$6.35e-03$	$1.94e-03$
2^{-18}	$8.23e-02$	$3.13e-02$	$1.48e-02$	$5.23e-02$	$1.93e-02$	$7.61e-03$	$3.00e-02$	$1.18e-02$	$3.85e-03$	$1.63e-02$	$6.94e-03$	$1.94e-03$
2^{-22}	$8.27e-02$	$3.14e-02$	$1.48e-02$	$5.27e-02$	$1.94e-02$	$7.61e-03$	$3.03e-02$	$1.19e-02$	$3.86e-03$	$1.65e-02$	$6.98e-03$	$1.94-03$

Table 4: Computed $\mathtt{E}_{\varepsilon,\theta}^{N,M}$ and $\mathrm{P}_{\varepsilon,\theta}^{N,M}$ for different ε, θ and s for Example 1.

Number of intervals in space and time						
		$N = 16$	$N = 32$	$N = 64$	$N = 128$	$N = 256$
s	(ε, θ)	$M = 10$	$M = 20$	$M = 40$	$M = 80$	$M = 160$
Present Approach						
0.2	$(2^{-6}, 2^{-18})$	$7.1577e-02$	$3.9198e-02$	$2.1401e-02$	$1.133e-02$	$5.8576e-03$
		0.869	0.873	0.918	0.952	–
	$(2^{-12}, 2^{-28})$	$7.7493e-02$	$4.2412e-02$	$2.2892e-02$	$1.1917e-02$	$6.0871e-03$
		0.870	0.890	0.942	0.969	–
Results in [26]						
	$(2^{-6}, 2^{-18})$	$7.8576e-02$	$6.9196e-02$	$4.7451e-02$	$2.8080e-02$	$1.5321e-02$
		0.183	0.544	0.757	0.874	–
	$(2^{-12}, 2^{-28})$	$1.1880e-01$	$7.3299e-02$	$4.1310e-02$	$2.2011e-02$	$1.1373e-02$
		0.697	0.827	0.908	0.953	–
Present Approach						
0.8	$(2^{-6}, 2^{-18})$	$6.1000e-02$	$3.8654e-02$	$2.1423e-02$	$1.1328e-02$	$5.8584e-03$
		0.658	0.851	0.919	0.951	–
	$(2^{-12}, 2^{-28})$	$7.7482e-02$	$4.2405e-02$	$2.2891e-02$	$1.1917e-02$	$6.0871e-03$
		0.870	0.890	0.942	0.969	–
Results in [26]						
	$(2^{-6}, 2^{-18})$	$7.8860e-02$	$4.4466e-02$	$2.3437e-02$	$1.2013e-02$	$6.0799e-03$
		0.827	0.924	0.964	0.983	–
	$(2^{-12}, 2^{-28})$	$1.4226e-01$	$7.7775e-02$	$4.0788e-02$	$2.0889e-02$	$1.0571e-02$
		0.871	0.931	0.965	0.983	–

contour and mesh plots in Figures 1, 3, 4, 6, and 7 for Examples 1 and 2, respectively. These figures clearly demonstrate the steep gradients of the numerical solution near the discontinuity points ($x = s$), particularly as the perturbation parameters ε and θ decrease. Such behavior is a direct indication of the presence of boundary and interior layers, a common feature in singularly perturbed problems involving discontinuous data. The sensitivity of the solution to the perturbation parameters is highlighted by the narrowing of these layers with decreasing ε or θ (see Figures 1a and 4a), underscoring the need for fitted mesh approaches for precise numerical resolution. Furthermore, Figures 3 and 6, which correspond to Examples 1 and 2, show surface plots for different discontinuity positions s. The line plots at various time levels

Table 5: Computed $\mathbb{E}_{\varepsilon,\theta}^{N,M}$ and $\mathbb{P}_{\varepsilon,\theta}^{N,M}$ when $\varepsilon = 2^{-8}$ for Example 2

θ $\downarrow$	$N=32$ $M=32$	$N=64$ $M=64$	$N=128$ $M=128$	$N=256$ $M=256$	$N=512$ $M=512$
1	$2.2303e-02$	$1.1082e-02$	$5.6730e-03$	$2.8751e-03$	$1.4485e-03$
2^{-2}	$2.2303e-02$	$1.1071e-02$	$5.6738e-03$	$2.8754e-03$	$1.4485e-03$
2^{-4}	$2.1148e-02$	$1.1066e-02$	$5.6735e-03$	$2.8754e-03$	$1.4485e-03$
2^{-6}	$2.1087e-02$	$1.1063e-02$	$5.6732e-03$	$2.8754e-03$	$1.4485e-03$
2^{-8}	$2.1095e-02$	$1.1064e-02$	$5.6730e-03$	$2.8754e-03$	$1.4485e-03$
2^{-10}	$2.1097e-02$	$1.1065e-02$	$5.6731e-03$	$2.8754e-03$	$1.4485e-03$
$\vdots$	$\vdots$	$\vdots$	$\vdots$	$\vdots$	$\vdots$
2^{-22}	$2.1097e-02$	$1.1065e-02$	$5.6731e-03$	$2.8754e-03$	$1.4485e-03$
2^{-24}	$2.1097e-022$	$1.1065e-02$	$5.6731e-03$	$2.8754e-03$	$1.4485e-03$
$\mathbb{E}^{N,M}$	$2.2303e-02$	$1.1082e-02$	$5.6738e-03$	$2.8754e-03$	$1.4485e-03$
$\mathbb{R}^{N,M}$	1.01	0.966	0.981	0.989	–
Result in [1]					
$\mathbb{E}^{N,M}$		$1.33874e-02$	$1.16318e-02$	$8.67966e-03$	$5.89059e-03$
$\mathbb{P}^{N,M}$		0.202	0.422	0.559	–

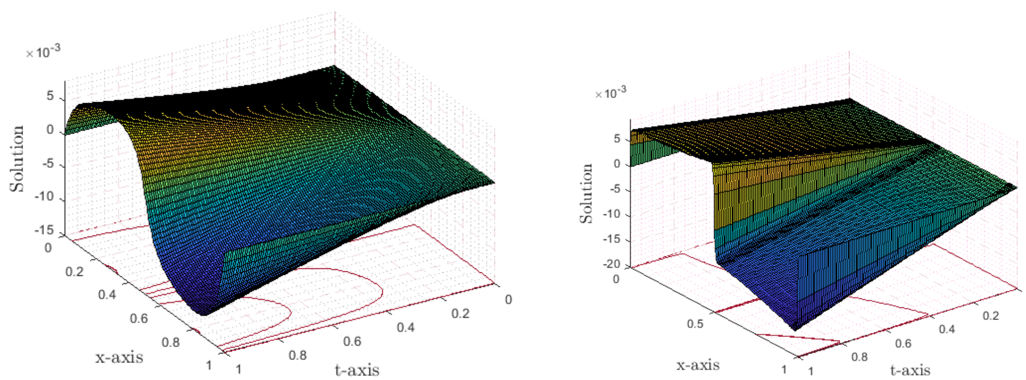

(a) $\varepsilon = 1, \theta = 2^{-10}$ (b) $\theta = 2^{-10}, \varepsilon = 2^{-8}$

Figure 1: The computed solution profiles for Example 1 using $N = M = 128$.

with $N = M = 128$ (Figures 2 and 5) show that the boundary and interior layer regions, where the solution profile varies quickly, are where the maximum numerical error is found. The plots also support the theoretical predictions about how layer thickness depends on perturbation magnitudes by showing that decreasing ε and θ results in sharper layer transitions. The results are in line with previous research presented in [21], which found that, under the condition that the source term $f(x,t)$ stays continuous, interior layers are mainly caused by discontinuities in the

Table 6: Computed $\mathtt{E}_{\varepsilon,\theta}^{N,M}$ and $\mathrm{P}_{\varepsilon,\theta}^{N,M}$ for different ε, θ and s for Example 2.

Number of intervals in space and time						
		$N = 16$	$N = 32$	$N = 64$	$N = 128$	$N = 256$
s	(ε, θ)	$M = 10$	$M = 20$	$M = 40$	$M = 80$	$M = 160$
Present Approach						
0.2	$(2^{-6}, 2^{-18})$	$5.6359e-02$	$3.1368e-02$	$1.6956e-02$	$8.8405e-03$	$4.5256e-03$
		0.869	0.873	0.918	0.952	–
	$(2^{-12}, 2^{-28})$	$5.8369e-02$	$3.2425e-02$	$1.7407e-02$	$9.0228e-03$	$4.5945e-03$
		0.848	0.897	0.948	0.974	–
Results in [26]						
	$(2^{-6}, 2^{-18})$	$6.7015e-02$	$6.1676e-02$	$4.3579e-02$	$2.6251e-02$	$1.4462e-02$
		0.120	0.501	0.731	0.860	–
	$(2^{-12}, 2^{-28})$	$3.7093e-02$	$2.8247e-02$	$1.8060e-02$	$9.9259e-03$	$5.2073e-03$
		0.393	0.645	0.864	0.931	–
Present Approach						
0.8	$(2^{-6}, 2^{-18})$	$5.2613e-02$	$3.1062e-02$	$1.7031e-02$	$8.9668e-03$	$4.6131e-03$
		0.760	0.867	0.926	0.959	–
	$(2^{-12}, 2^{-28})$	$5.8369e-02$	$3.2582e-02$	$1.7746e-02$	$9.2488e-03$	$4.7213e-03$
		0.841	0.877	0.940	0.970	–
Results in [26]						
	$(2^{-6}, 2^{-18})$	$5.6605e-02$	$4.4466e-02$	$1.7632e-02$	$9.0974e-03$	$4.6191e-03$
		0.779	0.904	0.955	0.978	–
	$(2^{-12}, 2^{-28})$	$3.9828e-02$	$3.1977e-02$	$1.9895e-02$	$1.0191e-02$	$5.1934e-03$
		0.317	0.685	0.965	0.973	–

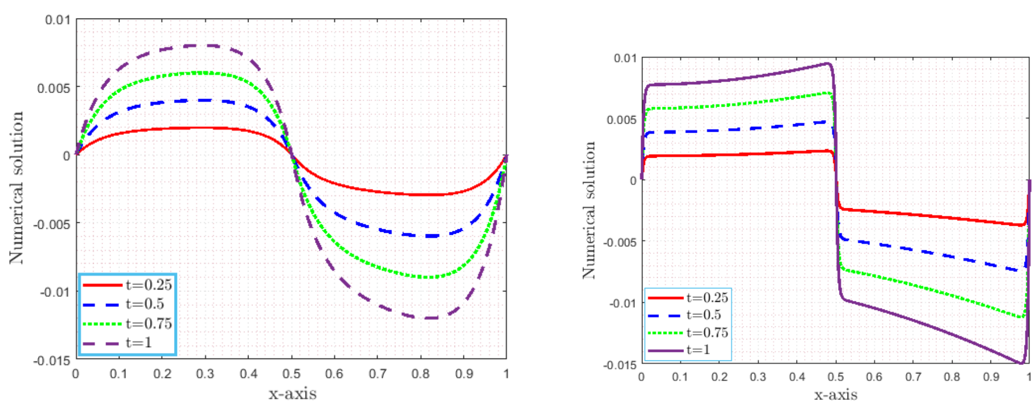

(a) $\varepsilon = 1, \theta = 2^{-10}$ (b) $\theta = 2^{-10}, \varepsilon = 2^{-8}$

Figure 2: Line plots illustrating Example 1 for several time increments.

convection coefficient. Our comprehension of the interaction between discontinuous coefficients and solution layer structures is improved by this numerical evidence. As can be seen in Figure 7, the resulting solution typically only shows boundary layers if the discontinuity only occurs in

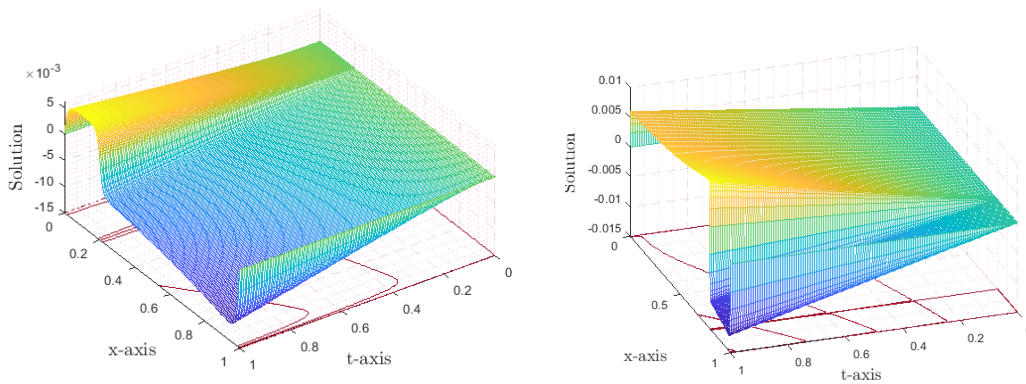

(a) $\varepsilon = 2^{-4}, \theta = 2^{-8}$ and $s = 0.2$ (b) $\theta = 2^{-8}, \varepsilon = 2^{-10}$ and $s = 0.8$

Figure 3: Computed solution profiles for Example 1 with $N = 256$ and $M = 160$, illustrating the influence of varying s values.

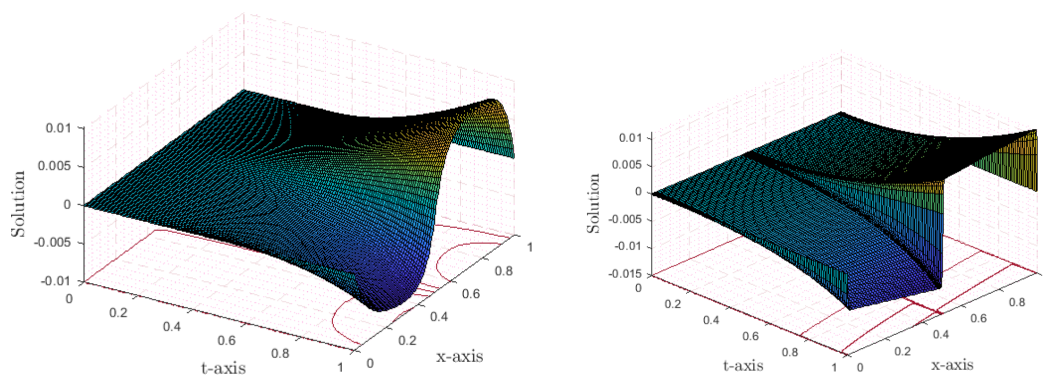

(a) $\varepsilon = 1, \theta = 2^{-12}$ (b) $\theta = 2^{-8}, \varepsilon = 2^{-10}$

Figure 4: The computed solution profiles for Example 2 using $N = M = 128$.

the convection coefficient (with a smooth $f(x,t)$). To further investigate this behavior, the discontinuous source term in Example 2 was replaced by the smooth functions $f(x,t) = (e^{t^2} - 1)(1 + xt)$ and $f(x,t) = -t^2(2 + x)$. The corresponding numerical results are presented in Figures 7a and 7b, respectively. The findings demonstrate that when the source term is smooth, no distinct interior layer forms, even though the discontinuity in the convection coefficient causes a shift in the layer position. This finding indicates that the emergence and intensity of interior layers are significantly influenced by discontinuities in the source term. Additionally, Figures 8a and 8b for Examples 1 and 2, respectively, show error distributions on a log-log scale to verify the theoretical convergence behavior of the proposed approach. These plots support the robustness

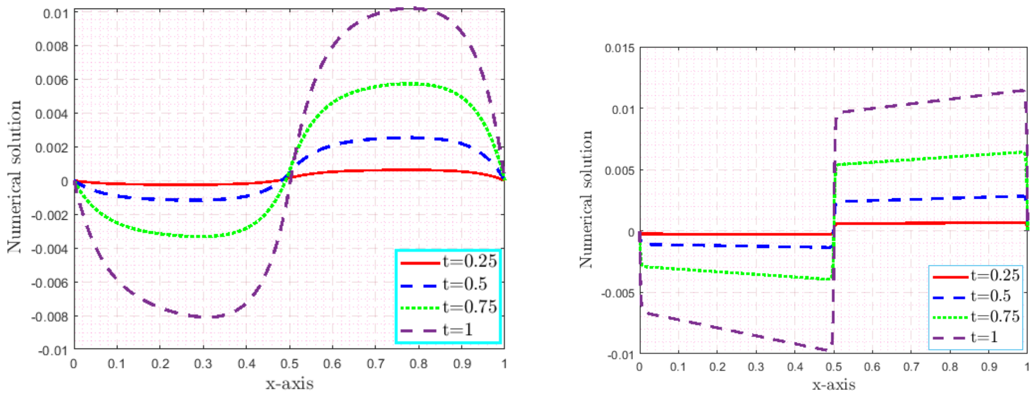

(a) $\varepsilon = 1, \theta = 2^{-12}$ (b) $\theta = 2^{-8}, \varepsilon = 2^{-10}$

Figure 5: Line plots illustrating Example 2 for several time increments.

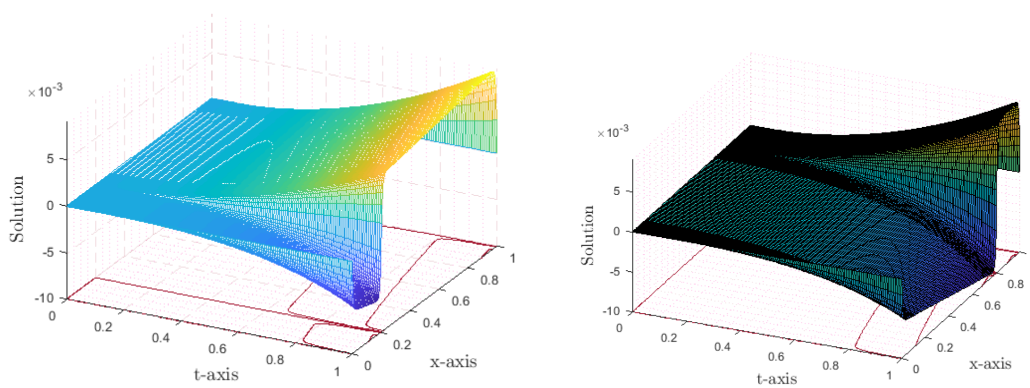

(a) $\varepsilon = 2^{-6}, \theta = 2^{-18}$ and $s = 0.2$ (b) $\theta = 2^{-18}, \varepsilon = 2^{-6}$ and $s = 0.8$

Figure 6: Computed solution profiles for Example 2 with $N = 256$ and $M = 160$, illustrating the influence of varying s values.

and (ε, θ)-uniform accuracy of the numerical scheme by confirming that it achieves the anticipated rate of convergence. These results have important ramifications for real-world applications in fluid transport, convection-diffusion processes, and semiconductor modeling, where abrupt gradients and discontinuities frequently occur naturally.

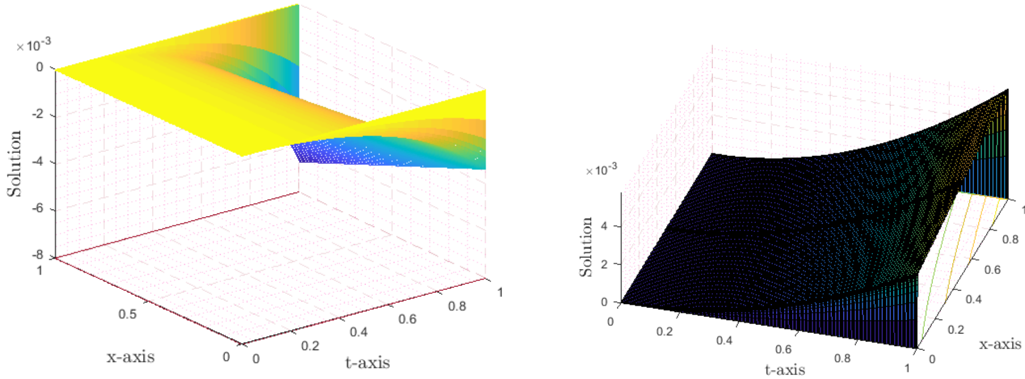

(a) $f(x,t) = \left(e^{t^2} - 1\right)(1 + xt)$ (b) $f(x,t) = -t^2\,(2 + x)$

Figure 7: Computed solution profiles for Example 2 with $N = M = 256$, $\varepsilon = 2^{-12}$, $\theta = 2^{-8}$, considering multiple continuous source terms.

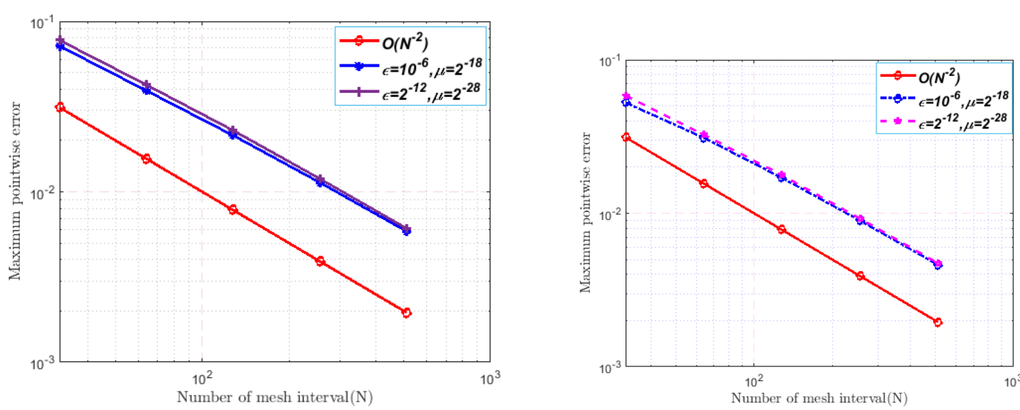

(a) Example 1 (b) Example 2

Figure 8: Loglog plot of Maximum pointwise errors.

6 Conclusion

An implicit numerical framework for solving a TP-SPPPs with discontinuities in the source and convection terms was presented in this work. It is based on a predefined Shishkin mesh. These issues were distinguished from situations involving smooth data by the complex solution behavior introduced by the existence of both boundary and interior layers. The suggested approach combined a cubic spline in tension for spatial approximation on a fitted mesh with the implicit Euler method for temporal discretization. Convergence analysis and extensive numerical experiments confirmed that the method achieves first-order accuracy in time and second-order accuracy up to a logarithmic factor in space and is uniformly stable and robust. As the perturbation parameters ε and θ decrease, the graphic results clearly show the emergence of parabolic boundary layers along the lateral edges and interior layers around $x = s$. The boundary subregions and steep gradients near the discontinuity location s showed how well the scheme captures layer behavior even under extreme perturbations. The reliability of the proposed approach was demonstrated by comparative studies, which yield accuracy that is on par with or better than that of existing methods. The method's resilience in handling discontinuous singular perturbation problems was demonstrated by both theoretical validation and empirical results.

Acknowledgements

Authors are grateful to there anonymous referees and editor for their constructive comments.

Funding

This research received no external funding.

Conflicts of Interest

The authors declare no conflicts of interest.

References

[1] Chandru, M., Das, P. and Ramos, H. *Numerical treatment of two-parameter singularly perturbed parabolic convection diffusion problems with non-smooth data*, *Math. Methods Appl. Sci.* 41(14) (2018), 5359–5387.

[2] Chandru, M., Prabha, T., Das, P. and Shanthi, V. *A numerical method for solving boundary and interior layers dominated parabolic problems with discontinuous convection coefficient and source terms*, *Differ. Equ. Dyn. Syst.* 27(1) (2019), 91–112.

[3] Chandru, M., Prabha, T. and Shanthi, V. *A parameter robust higher order numerical method for singularly perturbed two parameter problems with non-smooth data*, *J. Comput. Appl. Math.* 309 (2017), 11–27.

[4] Cheru, S. L., Duressa, G. F. and Mekonnen, T. B. *Robust numerical approach for singularly perturbed parabolic problems with discontinuous convection coefficients and source terms*, *Comput. Methods Differ. Equ.* (2025) (in press).

[5] Cheru, S. L., Duressa, G. F. and Mekonnen, T. B. *Gaussian quadrature method with exponential fitting factor for two-parameter singularly perturbed parabolic problem*, *BMC Res. Notes* 17(1) (2024), 1–7.

[6] Cheru, S. L., Duressa, G. F. and Mekonnen, T. B. *Robust numerical methods for two-parameter singularly perturbed parabolic problems with non-smooth data*, *Sci. Afr.* (2025), e03064.

[7] Cheru, S. L., Duressa, G. F. and Mekonnen, T. B. *Numerical integration method for two-parameter singularly perturbed time delay parabolic problem*, *Front. Appl. Math. Stat.* 10(15) (2024) 1414899.

[8] Clavero, C., Gracia, J. L., Shishkin, G. I. and Shishkina, L. P. *An efficient numerical scheme for 1D parabolic singularly perturbed problems with an interior and boundary layers*, *J. Comput. Appl. Math.* 318 (2017), 634–645.

[9] Daba, I. T., Melesse, W. G., Gelu, F. W. and Kebede, G. D. *An efficient numerical approach for singularly perturbed time delayed parabolic problems with two-parameters*, *BMC Res. Notes* 17(1) (2024) 158.

[10] Das, P. and Mehrmann, V. *Numerical solution of singularly perturbed convection–diffusion–reaction problems with two small parameters*, *BIT Numer. Math.* 56 (2016), 51–76.

[11] Farrell, P. A., Hegarty, A. F., Miller, J. J., O'Riordan, E. and Shishkin, G. I. *Global maximum norm parameter-uniform numerical method for a singularly perturbed convection–diffusion problem with discontinuous convection coefficient*, *Math. Comput. Model.* 40(11–12) (2004), 1375–1392.

[12] Gracia, J. L., O'Riordan, E. and Pickett, M. L. *A parameter robust second order numerical method for a singularly perturbed two-parameter problem*, *Appl. Numer. Math.* 56(7) (2006), 962–980.

[13] Kadalbajoo, M. K. and Jha, A. *Exponentially fitted cubic spline for two-parameter singularly perturbed boundary value problems*, *Int. J. Comput. Math.* 89(6) (2012), 836–850.

[14] Kaushik, A. and Sharma, M. *An optimal asymptotic-numerical method for convection dominated systems having exponential boundary layers,* J. Differ. Equ. Appl., 22(9) (2016) 1307–1324.

[15] Kumar, D. and Kumari, P. *Uniformly convergent scheme for two-parameter singularly perturbed problems with non-smooth data*, *Numer. Methods Partial Differ. Equ.* 37(1) (2021), 796–817.

[16] Kumar, D., Yadaw, A. S. and Kadalbajoo, M. K. *A parameter-uniform method for two parameters singularly perturbed BVPs via asymptotic expansion*, *Appl. Math. Inf. Sci.* 7(4) (2013), 1525.

[17] Kumar, P. M. M. and Ravi Kanth, A. S. V. *Computational study for a class of time-dependent singularly perturbed parabolic partial differential equation through tension spline*, *Comput. Appl. Math.* 39(3) (2020), 233.

[18] Linss, T. *A posteriori error estimation for a singularly perturbed problem with two small parameters*, *Int. J. Numer. Anal. Model.* 7(3) (2010) 491–506.

[19] Mukherjee, K. and Natesan, S. *An efficient numerical scheme for singularly perturbed parabolic problems with interior layer*, *Neural Parallel Sci. Comput.* 16(3) (2008), 405.

[20] O'Riordan, E., Pickett, M. and Shishkin, G. *Parameter-uniform finite difference schemes for singularly perturbed parabolic diffusion–convection–reaction problems*, *Math. Comp.* 75(255) (2006), 1135–1154.

[21] O'Riordan, E. and Shishkin, G. I. *Singularly perturbed parabolic problems with non-smooth data*, *J. Comput. Appl. Math.* 166(1) (2004), 233–245.

[22] Prabha, T., Chandru, M. and Shanthi, V. *Hybrid difference scheme for singularly perturbed parabolic problem with boundary and interior layers*, *Appl. Math. Comput.* 314 (2017), 237–256.

[23] Prabha, T., Chandru, M., Shanthi, V. and Ramos, H. *Discrete approximation for a two-parameter singularly perturbed boundary value problem having discontinuity in convection coefficient and source term*, *J. Comput. Appl. Math.* 359 (2019), 102–118.

[24] Schlichting, H. and Gersten, K. *Boundary-layer theory.* springer; 2016.

[25] Shanthi, V., Ramanujam, N. and Natesan, S. *Fitted mesh method for singularly perturbed reaction–convection–diffusion problems with boundary and interior layers*, *J. Appl. Math. Comput.* 22 (2006), 49–65.

[26] Singh, S., Choudhary, R. and Kumar, D. *An efficient numerical technique for two-parameter singularly perturbed problems having discontinuity in convection coefficient and source term*, *Comput. Appl. Math.* 42(1) (2023), 62.